Mapping the present-day chemical abundance structure of the Solar neighbourhood: O & Si

Kristiina Verro

Lund Observatory
Lund University

2017-EXA112

Degree project of 60 higher education credits (for a degree of Master)
May 2017

Supervisor: Thomas Bensby

Lund Observatory
Box 43
SE-221 00 Lund
Sweden

Abstract

Context. Large scale chemical abundance gradients in the Galactic disks, small-scale abundance structures, and the mean chemical abundance values in the Solar vicinity, are important constraints to Galactic chemo-dynamical formation and evolution models. The formation and evolution of stars, and interstellar gas and dust depends on the distribution and evolution of matter in the Galaxy. Therefore, metallicity structures within the Milky Way can be mapped from the abundance analysis of its gas and stars.

Data. A sample of 379 mostly spectral type B main sequence stars within 1.5 kpc radius from the Sun, was observed with the `MIKE` high-resolution spectrograph on the Magellan 6.5-m telescope on Las Campanas in Chile in 2007. Projected rotational velocities and photometric effective temperatures were determined for these stars by Bragança et al. (2012). B stars are good indicators for present-day cosmic abundances due to their short lifetimes. They preserve the interstellar medium abundances, which they were born from, in the photosphere, and they do not migrate far from their birth environment.

Aims. The purpose of this Master's project was to start mapping the present-day silicon and oxygen abundance structure of the Solar neighbourhood, by determining the stellar atmospheric parameters, and Si and O abundances, for the low-rotating (< 22 km s^{-1}) subsample. The thesis at hand is part of an international study aimed to determine the elemental abundances of B-type main sequence stars near the Solar vicinity and in the outer Galactic disk (Bragança et al. 2012, 2015; Garmany et al. 2015, Bragança et al. in prep.).

Methods. Line-profile fitting of Si, O and Balmer lines, with full NLTE synthetic spectra, and an iterative analysis methodology, was used to constrain stellar atmospheric parameters and elemental abundances at high accuracy and precision.

Results & Conclusions. With this Master's thesis, an extensive mapping the Solar neighbourhood has begun: stellar parameters, and Si and O abundances were established for 17 stars. The mean elemental abundance of the Solar neighbourhood of a 1.25 kpc radius, was found to be 7.42±0.13 dex for silicon and 8.73±0.06 dex for oxygen. The results are consistent with the cosmic abundance standard from Nieva & Przybilla (2012) within error-bars, and provide reliable present-day anchor points for Galactic chemical evolution models. However, the stars in our sample have on average smaller abundance values and the Solar neighbourhood seems to be more heterogeneous, than determined by Nieva & Przybilla (2012) study. Small scale abundance structures were not discovered, due to yet small sample size. In the future, other low-rotating stars in the observed stellar sample will be analysed, up to a $v \sin i \simeq 80$km s^{-1} limit. This would amount to about 100 stars. Combined with Gaia DR2 positions, and chemical abundances for the fast rotating B-type stars in the Solar vicinity (Cazorla et al. 2017), would provide an unprecedented view of the present-day Solar neighbourhood.

Populärvetenskaplig beskrivning

Vår galax, Vintergatan, innehåller bortåt 200 miljarder stjärnor av varierande åldrar och storlekar. Under en mörk och klar natt kan man se ungefär 2000 med blotta ögat. Detta är en liten del av det stora hela, men tillräckligt för att stimulera människors nyfikenhet. Vad är de gjorda av, och varför är de där de är? Enkla frågor, som har väldigt komplexa svar. Genom att kartlägga strukturen och den kemiska sammansättningen hos den unga nuvarande stjärnpopulationen i solens närhet avser detta arbete att besvara den första frågan och ge ytterligare ledtrådar till den andra. Vintergatans ursprung och utveckling finns bevarat i form av den kemiska sammansättningen och kinematiska egenskaperna hos dess stjärnor och gas, så genom att bestämma stjärnors kemiska sammansättning kan man få information om den miljö som de bildades från. Detta arbete har använt sig av massiva (2–16 $M_{\odot}$) huvudseriestjärnor för att bestämma den nutida ymnigheten av syre och kisel i solens närhet. Massiva stjärnor är utmärkta indikatorer för Vintergatans nutida kemiska sammansättning, av flera anledningar. För det första så har massiva stjärnor korta livstider, några miljoner till några tiotals miljoner år, att jämföras med Vintergatans ålder som är runt 13 miljarder år. För det andra så befinner de sig fortfarande på den plats de bildades, detta på grund av att de inte hunnit migrera nämnvärt på de få miljoner år de levt. För det tredje så är de väldigt luminösa, och således lätta att observera, vilket beror på att de har så höga temperaturer (10000–30000 K). Ymnigheten av olika grundämnen i atmosfärerna hos dessa stjärnor representerar den kemiska sammansättning som det interstellära mediet hade när de bildades.

Den nutida sammansättningen av olika grundämnen i solens närhet utgör viktiga randvillkor för galaktiska kemisk-dynamiska utvecklingsmodeller eftersom de man vill att de skall resultera i realistiska Vintergatsmodeller. Riktmärket för Vintergatan är solens närhet som är det område som kan studeras med största noggrannhet och precision, eftersom stjärnorna är näraliggande och enkla att observera. Mer än 370 näraliggande (inom en radie av 1.5 kpc) massiva stjärnor observerades för detta projekt år 2007. Grova uppskattningar för stjärnornas rotationshastigheter och effektiva temperaturer gjordes av Bragança et al. (2012). Denna Masteruppsats har som mål att bestämma stjärnparametrar (effektiv temperature, ytgravitation, projicerad rotationsgahstighet, mikro- och makroturbulenshastigheter) och grundämneshalter på ett konsekvent sätt för de stjärnor som har låga rotationshastigheter. De observerade spektrumen jämfördes med syntetiskt spektrum, som genererats med hjälp av modellatmosfärer och atommodeller, för att analysera formerna på spektrallinjer. En linje-för-linje-baserad anpassningsmetod för kisel, syre, och vätelinjer användes, och statistiska metoder för att bestämma stjärnparametrar och grundämneshalter.

Denna metod är väldigt tidskrävande - att analysera en stjärna tar några dagar upp till en vecka - men berikande. I detta Masterprojekt har 17 stjärnor i solens närhet analyserats för att kartlägga kisel- och syrehalter i solens närhet. Vi fann att solens närhet verkar vara aningen mindre homogen än vad som tidigare rapporterats. Dock så överensstämmer medelhalterna för solens närhet med tidigare liknande studier, samt med dessa grundämnens halter i solen. På grund av den kemiska utvecklingen i Vintergatan så borde yngre stjärnor generellt sett ha högre grundämneshalter än solen som är äldre. Dessa resultat antyder att solen bildades i de inre delarna av Vintergatan, som är mer berikade, och sedan migrerade till dess nuvarande position 8 kpc från Vintergatans centrum. Några småskaliga ymnighetsvariantioner kunde inte detekteras, antagligen beroende på det ännu begränsade antal stjärnor som analyserats.

Framtida planer innefattar att analysera alla stjärnor i samplet, upp mot 100 stjärnor. Med denna Mastersuppsats har det detaljerade kartläggandet av solens närhet börjat!

Contents

List of Figures

List of Tables

Chapter 1

Introduction

The story of the formation and evolution of the Milky Way galaxy is written into the chemical and kinematic properties of its stars and gas. Different sets of astronomical objects can be used to probe the Galaxy's[1] chemical structure of the present or of the past. The Master's thesis at hand begins mapping the present-day chemical abundance structure of the Solar neighbourhood (extending to 1.5 kpc from the Sun) with spectral type B main sequence stars, to provide Galactic chemo-dynamical formation and evolution models with observational boundary conditions. Over 370 mostly B stars were observed for this task, with the high-resolution `MIKE` spectrograph at the Magellan Clay 6.5 m telescope on Las Campanas observatory in Chile. This Master's study takes under analysis 17 low-rotating stars in the observed sample. Hydrogen, silicon and oxygen lines were fitted with synthetic spectra, which were based on a grid of NLTE line-blanketed model atmospheres, and NLTE line formation calculations. An iterative analysis methodology was used to constrain stellar parameters (effective temperature, surface gravity, projected rotational velocity, micro- and macroturbulent velocity), and silicon and oxygen abundances with high precision and accuracy.

The large observed dataset and the high precision and accuracy methodology, allows to review the chemical homogeneity (with fluctuations of less than 10% around the mean) of the Solar neighbourhood, reported from previous studies on the present-day tracers (e.g. Cartledge et al. 2004; Nieva & Przybilla 2012; Przybilla et al. 2008; Rodríguez & Delgado-Inglada 2011), as well as the mean abundance values (the cosmic abundance standard) of the Solar neighbourhood (Nieva & Przybilla 2012; Przybilla et al. 2008). In comparison to the earlier studies, the current Master's project uses superior NLTE model atmospheres and line formation calculations, $\log gf$ calibration to reduce systematic errors, as well as thorough random error estimation to reveal the true precision of abundance determination. This Master's project is part of an international study of B-type main sequence stars near the Solar vicinity (Bragança et al. 2012, and this Master's thesis), and in the outer Galactic disk (Bragança et al. 2015; Garmany et al. 2015, Bragança et al. in prep.), with the objective to provide Galactic chemo-dynamical formation and evolution models with best possible observational constraints for present-day chemical abundances.

[1] Throughout this thesis, the term "Galaxy" is used as a synonym for Milky Way, in contrary to "galaxy", which is a general term.

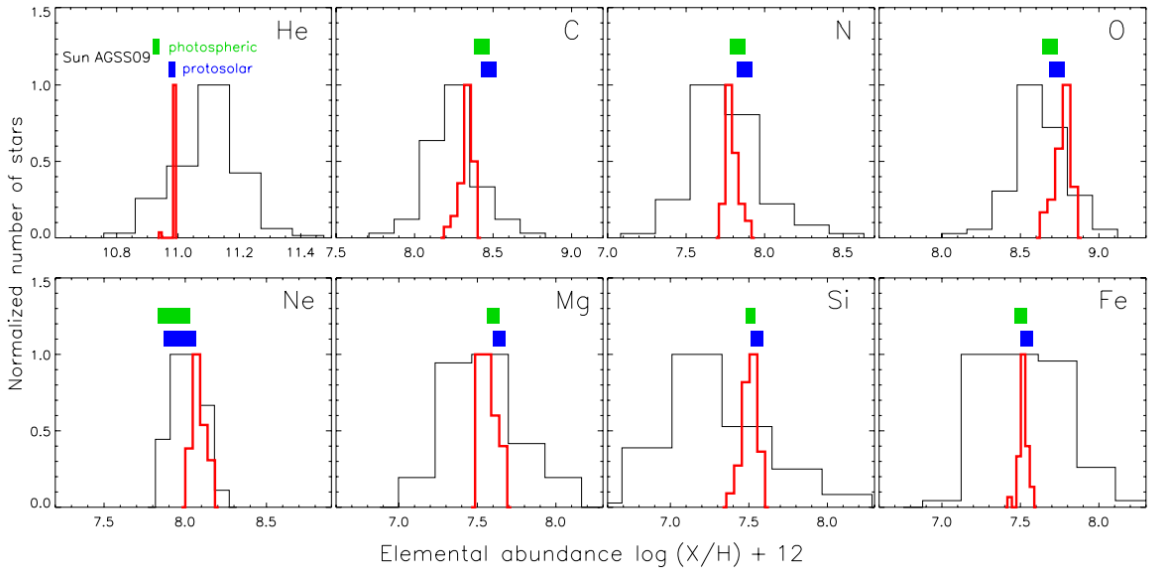

Figure 1.1: Abundance distributions in the Solar neighbourhood. Red: abundances determined from early B-type stars by Nieva & Przybilla (2012); black: literature data; Photospheric and proto-Solar abundances from Asplund et al. (2009), with the bars representing the $\pm 1\sigma$ uncertainties. Figure from Nieva & Przybilla (2012).

The present-day Galactic abundance structures were first studied through H II regions (Churchwell & Walmsley 1975). These large, low-density clouds of partially ionized gas are regions in which star formation has recently taken place, and they truly probe the current state of abundance values. Many studies of H II regions in optical and infrared wavelengths have since followed, with spatial reach from the Galactic centre (Martín-Hernández et al. 2002) to the outer parts of the disk (Deharveng et al. 2000; Esteban et al. 2005; Martín-Hernández et al. 2002; Rudolph et al. 2006). However, H II regions show large scatter in abundances at given Galactocentric distance, and a difference of 0.25 dex in abundances derived from optical data and infrared (Rudolph et al. 2006). Abundances from the diffuse interstellar medium (ISM) itself can be measured from lines of sight when observing a massive star (André et al. 2003; Cartledge et al. 2004, 2006; Oliveira & Hébrard 2006). Stars can be used as tracers of present-day abundance structures, assuming the lifetime of the star is much shorter than that of the Galaxy. This is true for massive stars, from about 5 $M_\odot$, as they have lifetimes in millions to tens of millions of years. Also, during this relatively short period, they do not have time to migrate far away from their birth environment. This makes them represent the present-day situation in a specific region of the Galaxy. Spectral type B main sequence stars (2–16 $M_\odot$) have proved to be excellent tools for studying the present-day chemical composition of the Galaxy, in the solar vicinity, as well as at great distances. B stars have been used as tracers of present-day cosmic abundances for decades. In 1942, the spectrum of a B-star was compared with a theoretical spectra for the first time. This was done in by Unsöld (1942), who studied the spectra of τ Sco. From that time onwards, several studies have targeted nearby B-type main sequence stars with the methods of stellar spectroscopy with growing complexity. Earlier studies (see overview by Morel 2009) showed the Solar neighbourhood

to be rather heterogeneous (up to 0.5 dex) and indicated lower abundances than the Solar standard. These studies were then revealed to be afflicted by systematic effects due to a poor determination of the stellar parameters and to the assumptions in the abundance analysis (e.g LTE model atmospheres and line formation calculations) (Przybilla et al. 2008; Simón-Díaz 2010). The latest study by Nieva & Przybilla (2012) analysed 29 B stars with a thorough and self-consistent analysis technique, and found the present-day Solar neighbourhood to be homogeneous, with abundance fluctuations of less than 10% around the mean. Figure 1.1, from their study, illustrates the improvement in the precision and accuracy in the determination of elemental abundances of B stars. The current Master's project aims to investigate this homogeneity with 17 low-rotating B-type stars, and high precision and accuracy methods, but conservative error estimation. A follow-up study of additional 80 low-rotating stars, and ongoing study of fast-rotating stars (Cazorla et al. 2017), promises to provide an unprecedented view of the present-day Solar neighbourhood. As massive stars are very bright, they can be observed from large distances. Studies by Bragança et al. (2015); Daflon & Cunha (2004); Rolleston et al. (2000); Smartt et al. (2001) and Bragança et al. (in prep.) have targeted more distant B stars to determine the large-scale abundance gradients of the present-day Milky Way. Although the current study used B-spectral type stars as the tracers, the present-day Galactic abundance structures could also be studied through Cepheids. These intermediate-mass stars (5–12 $M_{\odot}$) have turned off the main-sequence and are in the instability phase. The pulsation period of these variables are linked to their luminosity, so their distances can be determined accurately. The abundance structure of the Galaxy has been studied extensively using Cepheids (Andrievsky et al. 2004; Luck & Lambert 2011, and other articles in the series). However, the abundance values derived from Cepheids might be affected by internal mixing, when CNO-material is being dredged up.

Generally, all young astronomical objects probe the present of the Milky Way, as old objects represent the past. Hence, all types of low mass main sequence stars, Solar-type stars among them, are used in Galactic archaeology (e.g. Bensby et al. 2014; Bergemann et al. 2014; Gilmore et al. 2012), to understand the past of the Milky Way. The chemical abundances of the Sun have been determined with the highest accuracy and precision (Asplund et al. 2009), being the closest star. These Solar values might not define chemistry of the current area called "Solar neighbourhood", as stars migrate considerable distances during their lifetimes. The abundances of the Sun and Solar-type stars in the Solar vicinity can reveal the extent of radial migration and chemical enrichment in the Galaxy, when compared to the present-day Solar neighbourhood abundances (e.g. Spina et al. 2016). It has been suggested, that the Sun has migrated from the inner Galactic disk, with the the most likely birth-place to be between $4.4 < r < 7.7$ kpc (Minchev et al. 2013). However, low-mass stars can only be observed near the Solar vicinity, as they are with relatively low luminosities. After the main sequence phase, stars move up on the luminosity scale on the Hertzsprung-Russell diagram, evolving to the red giant branch. Red giants are the probes of the past and the present, as they represent stars with different ages and metallicities. Their high luminosity makes them observable to large distances, and they are even brighter in the near-infrared than in the optical wavelengths, which makes them good objects for studies aimed towards the dust-obscured parts of the Galaxy. Red giants have been used as tracers of Galaxy's chemical and physical structure in numerous studies, like Alves-Brito et al. (2010); Casagrande et al. (2016). Now, the Apache Point Observatory Galactic Evolution Experiment (APOGEE) has constructed a database of high-resolution ($R \sim 22500$) NIR spectra for over 10^5 mostly red giant branch,

and other luminous post-main-sequence stars, across the Milky Way (Majewski et al. 2015). This has led to a new wave of studies using red giant stars to map the chemo-dynamical past of the Milky Way (e.g. Anders et al. 2017; Cunha et al. 2016; Fernández-Alvar et al. 2017). Estimation of exact ages of red giant stars is still an active research topic, as ages of stars cannot be directly measured, and so are always model-dependent. Uncertainties in age estimation are still about 25%–40% (Anders et al. 2017; Martig et al. 2016). Elemental abundances in the Galaxy can be also traced back from $\sim 3 \cdot 10^7$ yr to 10 Gyr with studying planetary nebulae (PNe), as their progenitors had masses of about 1–8 $M_\odot$ (Stanghellini & Haywood 2010). Attempts have been made to further divide studied PNe by their ages and to determine separate abundances for each the epochs (Chiappini et al. 2009; Henry et al. 2010; Stanghellini & Haywood 2010).

Despite the tracer under study, the challenge has been to put the derived abundances into a temporal and spatial map of the Galaxy. Position determination for the tracers is the reason why one can talk about the stellar structures in the Milky Way. The ongoing European Space Agency's Gaia mission promises to bring clarity with providing "unprecedented positional and radial velocity measurements with the accuracies needed to produce a stereoscopic and kinematic census of about one billion stars in our Galaxy and throughout the Local Group"[2], with it's first data released in September 2016 (Gaia Collaboration et al. 2016a,b; Lindegren et al. 2016). Gaia mission follows the ESA Hipparcos satellite (launched in 1989[3]), that was the first space mission dedicated to such measurements (Perryman et al. 1997; van Leeuwen 2007).

Probing the Galaxy has led to characterization of four major stellar structure components – the bulge, the stellar halo, the thin, and the thick disk, which are distinguished by the ages, metallicities and kinematic properties of its stars. The distinction between these different stellar structure components comes from observations, but the knowledge about the formation and evolution comes from modelling and simulations. Simplest Galactic models assume the ejecta from dying stars are instantly mixed into the interstellar medium, from which a new generation of stars is born, but advanced chemo-dynamical models (e.g Chiappini et al. 2001; Minchev et al. 2013, 2015) try to treat the dynamics of gas, stars and dark matter, to find the relations between the four structure components. At the same time when chemo-dynamical models grow in sophistication, our understanding of the four structures based on observations grows more complex, providing boundary conditions as well as new challenges for the models. For example, observations have revealed a boxy/peanut-shaped bulge, with a complex stellar population, which is now being mapped with increasing accuracy (Bensby et al. 2017; Portail et al. 2015; Wegg et al. 2015). The stellar halo exhibits two sub-components – inner and outer stellar halo, that show different spatial density profiles, stellar orbits and metallicities (Carollo et al. 2007; Fernández-Alvar et al. 2017, and references therein). Additionally, recent spectroscopic observations in the Milky Way suggest that the thick disk has a significantly smaller scale-length than the thin disk (Bensby et al. 2011), which is not seen in other galaxies (Minchev et al. 2015).

The importance of the observed present-day abundance structure in the Solar neighbourhood is illustrated on Figure 1.2, where the oxygen gradient from the latest chemo-dynamical mod-

[2] http://sci.esa.int/gaia/
[3] https://www.cosmos.esa.int/web/hipparcos

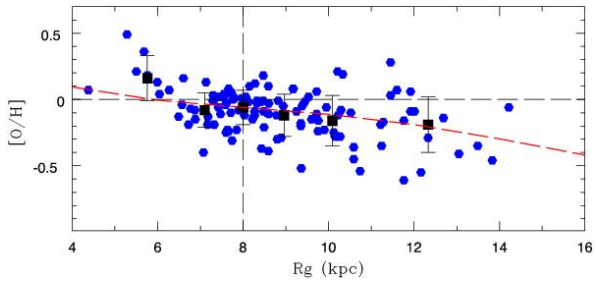

Figure 1.2: Abundances of oxygen as a function of galactocentric distance. The blue dots are the abundances from Cepheids (Andrievsky et al. 2004). The black squares represent the mean values inside each distance bin with standard deviations. The red dashed line shows the prediction of Minchev et al. (2013) model, normalized to the mean value of the Cepheids at the galactocentric distance of the Sun. Figure is taken from Minchev et al. (2013).

elling (Minchev et al. 2013) is compared to the observed present-day abundance values from Cepheids from Andrievsky et al. (2004). The prediction of the model itself is normalised to the oxygen abundance value of Cepheids in the Solar vicinity. The Solar neighbourhood represents the area in the Galaxy, which can be studied with the highest precision and accuracy, as the objects can be observed with high signal to noise ratio. This leads to highest quality measurements of the stellar parameters and chemical abundances. The Solar neighbourhood is not rigidly defined term, but varies from a few parsec to a few kiloparsec radius around the Sun, depending on the study. Studies in the pre-Gaia era used astrometry from Hipparcos mission, so this mission defined the reach of the "benchmark area" in the Milky Way. The new Gaia mission promises more exact positions in the Solar neighbourhood, as well as to extend the benchmark bubble. In this study, the Solar neighbourhood extends to 1.5 kpc from the Sun.

The thesis is structured as follows. Chapter 2 gives a short introduction to the properties of B-type mains sequence stars and describes the underlying models and assumptions for quantitative spectral analysis. Chapter 3 describes the observational data and Chapter 4 the used methodology for analysing the dataset. Chapter 5 contains the results and discussion, followed by a conclusion in Chapter 6.

Chapter 2

Properties of B-type stars

This Master's thesis uses B-type main sequence stars to determine present-day cosmic abundances in the Solar neighbourhood with the methods of stellar spectroscopy. Section 2.1 introduces the two chemical elements under study. In Section 2.2, the motivation for using B spectral type stars as representatives of present day Galaxy environment is given. Following sections give a short overview of how to decode a spectrum, using the stellar atmosphere and spectral line formation theories. These two theories are connected and need to be handled together. Detailed overview of the theory of stellar structure, and the nuances of stellar spectroscopy is beyond the scope of this work; for more details, see Gray (2005); Prialnik (2015) and lecture notes from the School of Spectroscopic Data Analyses (Catanzaro 2014; Kubát 2014; Ryabchikova 2014, etc.) available online[1].

2.1 Oxygen and silicon

Oxygen is the third most abundant element in the Universe, after hydrogen and helium. It is an α-process element, that is produced when carbon combines with He:

$$^{12}_{6}\mathrm{C} + ^{4}_{2}\mathrm{He} \rightarrow ^{16}_{8}\mathrm{O} + \gamma$$

Silicon is produced through oxygen burning, but is also an α-element:

$$^{16}_{8}\mathrm{O} + ^{16}_{8}\mathrm{O} \rightarrow ^{28}_{14}\mathrm{Si} + ^{4}_{2}\mathrm{He}$$
$$^{24}_{12}\mathrm{Mg} + ^{4}_{2}\mathrm{He} \rightarrow ^{28}_{14}\mathrm{Si} + \gamma$$

They are synthesized in stars before the silicon fusing process, and during Type II supernovae (Prialnik 2015). α-elements are important tracers of Galactic chemical evolution. For example, [α/Fe] vs. [Fe/H] comparison reveals information about the star formation rate and the initial mass function of the Galaxy, as seen on Figure 2.1. The knee in the [α/Fe] is caused by the delay time for the onset of Type Ia supernovae. Before the formation of the knee, core-collapse supernovae are the primary source of metals in the interstellar medium. After the knee, Type Ia supernovae begin to contribute metals, but by enriching with the iron-peak elements, so lowering the [α/Fe] ratio (McWilliam 1997).

[1] http://link.springer.com/book/10.1007/978-3-319-06956-2

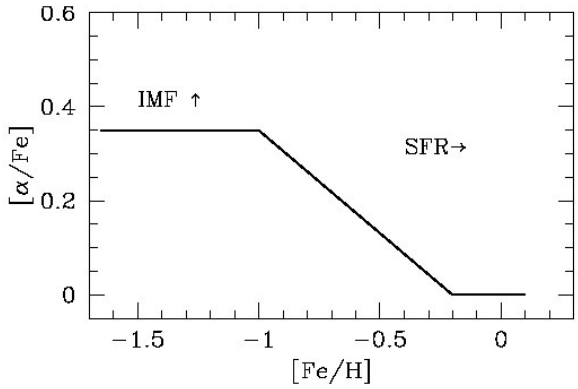

Figure 2.1: A scheme of the trend of α-element abundance with metallicity. Increased initial mass function and star formation rate affect the trend in the indicated directions. Figure is taken from McWilliam (1997).

Oxygen and silicon are the subjects of the thesis at hand, due to being good elements to build the stellar parameter estimation around. Massive stars show many strong O I, O II and O III, and Si II, Si III and Si IV lines in the optical spectra. As the methodology described in Chapter 4 takes advantage of Si and O lines to derive most of the stellar atmospheric parameters, it is convenient to start determining stellar abundances from these two elements before others.

2.2 Spectral type B main sequence stars

The classification of stars into O, B, A, F, G, K, M spectral types is based on behaviour of spectral lines depending on the temperature of the star. B-stars are massive stars ($2-16\ M_{\odot}$) with surface temperatures 10000–30000 K. The spectral characteristics of B-type stars are the weakening of He I lines and strengthening of Balmer lines with declining temperature. These characteristics make B stars good tracers of present-day cosmic abundances of the Galaxy for several reasons. First of all, in the terms of cosmic ages, B stars are born in the "present-day" Milky Way. Because of their high mass and the $\tau_{\rm MS} \propto M^{(1-\nu)}$ relation ($\nu \sim 3.5-4$ for massive stars), the more massive B-type main sequence stars (from about 6 $M_{\odot}$) have short main sequence lifetimes: from a few millions to a few tens of millions years. In comparison, the Sun, a low mass star, has been on the main sequence for 4.56 Gyr, and the oldest stars are as old as the Galaxy itself. Secondly, B stars are situated still near their birth environment, as they have not had time to migrate. Thirdly, B stars can be observed to large distances with high signal-to-noise ratios. B-star are very luminous due to their high temperatures ($L \propto T_{\rm eff}^4$). This allows them to be used as tracers of large scale present-day chemical abundance gradients, as well as of the small scale structures in the Solar vicinity. Lastly, spectral type B main sequence stars keep the pristine abundances in their photosphere. B-type stars, unlike the more massive O-type stars, or very low mass stars, do not have large internal convective zones, that would dredge up the elements from deep inside the star. This is an important characteristic, as dredge up would result in higher abundance values, which would then be interpreted as the initial ISM abundances.

2.3 Model atmospheres

This study used metal line-blanketed, NLTE, plane-parallel, hydrostatic model atmospheres. The following Section describes these terms and gives the motivation of using them in the context of spectral type B stars.

- Any star is balancing gravitational force with force from total pressure gradient at all times, and so is in **hydrostatic equilibrium**.

$$\frac{dP}{dx} = \rho g \ , \tag{2.1}$$

  where g is gravitational acceleration, ρ is the gas density, P is the total pressure and x in the geometrical depth.

- In a stellar atmosphere, the energy is carried by radiation, but not by convection or conduction. Following, the total radial energy flux (F_ν) travelling outward through the atmosphere should be constant in time and direction in a plane-parallel atmosphere, and the total energy flux is taken equal to the radiative flux through the atmosphere. The star is in **radiative equilibrium**:

$$\int_0^\infty F_\nu(\tau_\nu) d\nu = \sigma T_{\rm eff} \tag{2.2}$$

- **Line blanketing** takes into account the effect of line formation on the atmospheric structure. Spectral lines, in essence, are a signs of continuum energy redistribution. The large number of spectral lines influences the temperature distribution of the atmosphere, and so the spectral energy distribution. The effect of line opacity on the atmosphere is complicated, but generally the continuum producing deep layers of the star are heated, and the line forming regions cooled, when compared to a atmosphere in a line-free case. The high opacity of line frequencies does not contribute much for the outward flow of radiation. Thus, the temperature in these deeper layers must be higher compared to the line-free case ("backwarming"), to preserve the radiative equilibrium (2.2). In higher atmosphere layers, due to lower particle density, these frequencies become optically thin and start contributing to the outward radiation flow, which results in "surface cooling". Line blanketing can be taken into account with Opacity Distribution Functions (ODF), or Opacity Sampling (OS), which in essence are opacity maps for small frequency intervals. See Carbon (1979, Ch. 2) for an overview of line blanketing effects and handling.

- **Plane-parallel** atmosphere is a simplification where the physical properties depend on the vertical depth of the atmosphere only, and is based on the fact that the atmosphere of a B-type star is thin with respect to the radius of the star. This assumption reduces computational needs greatly, but does not describe the turbulent motions in the stellar atmosphere. To correct for this, two *ad hoc* parameters are created: micro- and macroturbulent velocities, that are discussed in Section 2.4. This may change in the future, as modern supercomputers already allow to calculate 3D hydrodynamic model

atmospheres, e.g. the Stagger-grid – a comprehensive grid of 3D model atmospheres for late-type stars (Magic et al. 2013, and other articles in the series). Luckily, the photospheres of B-type stars are not affected by strong stellar winds, unlike O-type stars, or by convection, unlike the cooler stars. Thus, B stars are well represented by plane-parallel 1D-models.

- Local thermodynamic equilibrium (LTE) approximation determines the behaviour of atomic level population and can be used when collisional processes dominate over radiative processes in the atmosphere. Then the ratio of the emission coefficient to the absorption coefficient (the source function), can be described by the Planck function and the velocities of particles follow the Maxwell distribution. Additionally, excitation and ionization states follow the Saha-Boltzmann distribution, corresponding to local values of temperature and gas pressure:

$$\frac{N_{n,i}}{N_{n,j}} = \frac{g_i}{g_j} e^{-(E_i - E_j)/kT)} \tag{2.3}$$

$$\frac{N_{n+1}}{N_n} = \frac{1}{N_e} \frac{2g_{n+1}}{g_n} \left[\frac{2\pi m_e kT}{h^2}\right]^{3/2} e^{-(\frac{E_n}{kT})} \tag{2.4}$$

where N_n and N_{n+1} are the populations on the ground level of ionization stage n and $n+1$; $N_{n,i}$ and $N_{n,j}$ populations of two levels of the same ionization stage; N_e is the electron number density. E_i and E_j are the energy of the lower and upper levels of transition, E_n is the ionization energy, $g_i = 2J + 1$ is the statistical weight of level i (J is the total angular momentum quantum number), m_e is the mass of electron, k is the Boltzmann constant. However, kinetic equilibrium or **non-LTE (NLTE)** is more general than the assumption of LTE, as there is no assumption made by the shape of the source function. The radiation field distribution is determined from the solution of the radiative transfer equation – source function is calculated from actual opacities and emissivities. LTE approximation allows relatively simple and fast calculation of excitation and ionization states, but for NLTE, these are calculated assuming statistical equilibrium (Equation 2.5), which include the non-local influence of radiation on level populations. In NLTE, the particle velocities are still assumed to follow Maxwell distribution. The validity of using the LTE approximation is determined by whether collisional or radiative processes are dominant in the atmosphere. The atmospheres of B-type stars are dominated by radiation processes, so NLTE handling of line formation and model atmospheres is needed.

- **Statistical equilibrium** (Equation 2.5) assumes, that there is a balance between the total number of transitions out and into atomic level i from other levels j, taking into account the collisional (C_{ji}) and radiative rate (R_{ji}). Additionally, when assuming global electrical neutrality in the atmosphere (Equation 2.6), electron density can be determined. This is a charge conservation law that takes into account charge (Z_i) from all levels of all ions of all species.

$$N_i \sum_{i \neq j} (R_{ij} + C_{ij}) = N_j \sum_{j \neq i} (R_{ji} + C_{ji}) \tag{2.5}$$

$$\sum_i N_i Z_i - N_e = 0 \tag{2.6}$$

2.4 Line formation and line broadening

In stellar spectroscopy, the term *model atom* is used for a dataset of energy levels (or groups of levels, so called superlevels), continuum transitions and line transitions for a specific atom or ion.

A spectral line is created when an atom or an ion with certain properties absorbs a photon with a certain wavelength in the stellar atmosphere, resulting in excitation of the atom/ion. Excited atom/ion can then de-excite and emit a photon with some characteristic wavelength. The amount and strength of spectral lines, as well as their position in the wavelength scale, is determined by atmospheric and atomic properties, like the upper and lower level populations for a transition, statistical weights of these levels, the probabilities of spontaneous emission and absorption, and simulated emission of photons with certain frequency. In line formation calculations, LTE approximation could be used. However, many spectral lines in the spectrum of B stars, silicon and oxygen lines among them, are found to deviate from their LTE-calculated synthetic lines, so NLTE handling is needed (e.g. Przybilla et al. 2011).

The strength of the line is usually described by the equivalent width (W_λ), or by the reduced equivalent width ($\log \frac{W_\lambda}{\lambda}$). W_λ is found by forming a rectangle with a height from the base of the line to the continuum emission, and finding the width of the rectangle, that has an area equal to the area of the spectral line.

In reality, the absorption line profile is a product of the central line absorption, and the absorption profile. The latter is a convolution of different widening profiles (see comparison of Gaussian, Lorentzian, Elliptical and Holtsmark profiles on Figure 2.2). Which profile is more dominant in the convolution, is determined by the influence of spectral line broadening agents listed below.

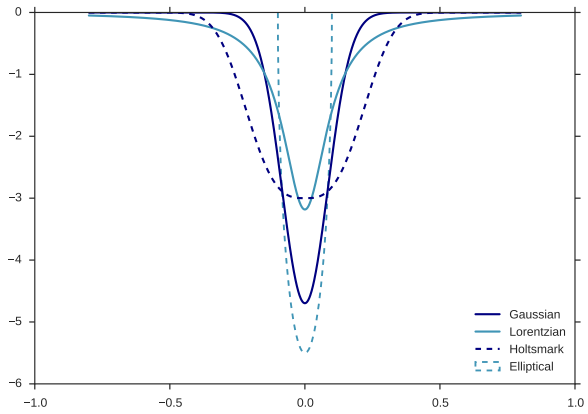

Figure 2.2: Elliptical, Holtsmark, Gaussian and Lorentzian line profiles.

Natural broadening

The lifetime of an excited state is limited by spontaneous de-excitation. This is governed by a transition probability from upper to lower energy state per second per particle in upper state. Excited states have a finite lifetime, but by the time–energy uncertainty principle, short lifetime will have a large energy uncertainty. Each time excited state decays, the energy they release is slightly different and thus spectral lines have a "natural" width, which follows the Lorentzian profile.

Pressure broadening

Closeness of charged particles in the stellar atmosphere momentarily perturb the energy levels of an atom through Coulomb interaction. The frequency of a bound-bound transition between these perturbed levels is thus affected, with the energy change proportional to the surrounding field strength. Neutral hydrogen has a permanent dipole moment, due to having only one electron, so its energy levels can easily be perturbed with interactions with charged particles, like protons and electrons. This is called linear Stark effect and is an important widening parameter in hot stars, where excitement of hydrogen atoms becomes important. Hot stars have very wide Balmer lines, as seen on Figure 2.3. Linear Stark broadening has a Lorenzian or Holtsmark profile, depending on whether the perturber is an electron or a proton. For lines other than neutral hydrogen and hydrogen-like atoms, quadratic Stark mechanism takes effect. These atoms are broadened by short spatial extent collisions with electrons. The broadening function is a Lorentzian.

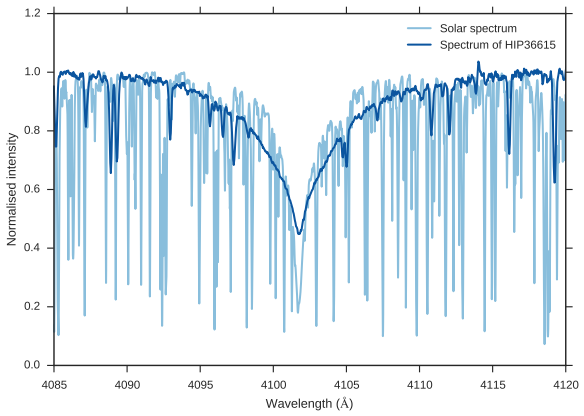

Figure 2.3: Hδ line in HIP36615 and Solar spectrum[2].

Although linear and quadratic Stark broadening effects are the most important pressure-caused widening mechanisms in hot stars, there are also others. Van der Waals effect affects cool stars, because it has neutral hydrogen, which in cool stars has not been ionized yet, that acts as the perturber for non-hydrogenic lines. Resonance broadening affects Solar-type stars, and it arises from the interaction between neutral hydrogen atoms themselves. All these widening effects happen due to collisions or close encounters of particles in a stellar

[2]Solar spectrum is taken from BASS2000 Solar Survey Archive: http://bass2000.obspm.fr/solar_spect.php

atmosphere. The more compressed the star is, the more effect the pressure broadening agents have.

Doppler broadening

The along the line of sight motion of the radiating atom/ion produces a Doppler shift in the observed photon. Photon is blueshifted when the particle moves upward in the stellar atmosphere, and redshifted when downward. Doppler shift can be caused by thermal movements and turbulence in the atmosphere, but also by rotational velocity of the star. The particle velocities follow a Maxwell distribution and the thermal motions broaden the line in a manner, that follows a Gaussian profile. When assuming time-independent plane-parallel geometry of the stellar atmosphere, the turbulent motions are not taken into account. To make up for the deficiency of the models, two parameters have been created: microturbulence and macroturbulence. They are *ad hoc* parameters, assumed to have random nature and describe microscopic scales and macroscopic scales, respectively. Microturbulence (ξ) is defined as an addition to the thermal broadening:

$$\Delta\nu_D = \frac{\nu_0}{c}\sqrt{\frac{2kT}{m} + \xi^2} \tag{2.7}$$

where ν_0 is the central frequency, m is the mass of the particle. Macroturbulence (ζ) is added by convolving the computed emergent intensity profile numerically by a Gaussian velocity distribution component $\Theta(\Delta\lambda)$:

$$I_(\nu) = I^0_\nu * \Theta(\Delta\lambda) \tag{2.8}$$

The rotation of the whole star also causes broadening of spectral lines. In B-type main sequence star, this becomes very relevant. As we see the star in a certain angle respect to the rotational axis, the lines are broadened by the projected rotational velocity $v \sin i$, where i is the inclination angle. This has an elliptical broadening profile. If the stellar surface would be resolved, spectral lines observed from different points of the star would be either blue- or redshifted. When observing stars as point-sources, the resulting effect is broadening in both directions. Figure 2.4 shows He I 4388 Å line for two stars: HIP36615 ($v \sin i = 3$ km s^{-1}) and HIP29121 ($v \sin i = 364$ km s^{-1}). Spectra of stars with high $v \sin i$ cannot be analysed, as even strong lines like He I have broadened to the extent of blending in with the continuum.

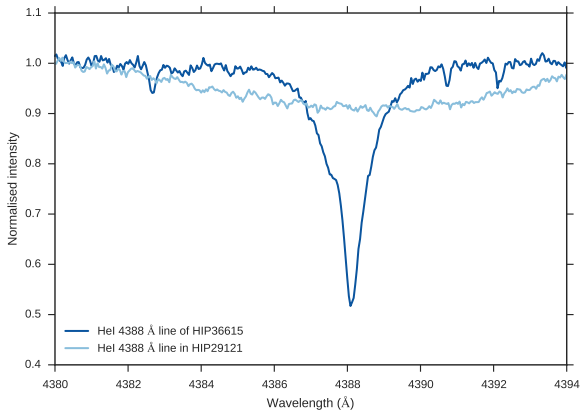

Figure 2.4: He I 4388 Å line in HIP36615 ($v \sin i = 3$ km s^{-1}) and HIP29121 ($v \sin i = 364$ km s^{-1})

Resolution and instrumental profile

The spectrograph itself puts limits to measuring very narrow spectral lines, via the finite resolution of the spectrograph and the instrumental profile. Resolving power[3] is defined as:

$$R = \frac{\lambda}{\Delta\lambda} \tag{2.9}$$

where $\Delta\lambda$ is the still resolved smallest wavelength interval (the resolution), from the Rayleigh criterion of diffraction of light in the spectrograph, and λ is the actual wavelength. The broadening mechanism coming from the finite resolution is the instrumental profile. The instrumental profile is a Gaussian profile, with the full-width at half maximum (FWHM) equal to $\Delta\lambda$ in perfect cases. The instrumental profile can be measured from the spectrum of the telescope's internal calibration lamp, as the spectral lines of the lamp are not affected by other broadening agents than natural and instrumental broadening. The light from the lamp has to travel through the spectrograph onto a CCD, during which it gets additional broadening that is described by the instrument's line profile. Usually, FWHM $> \Delta\lambda$, as the FWHM of the Gaussian also measures other broadening processes – from scattering within optical elements to diffraction in optical edges. The FWHM can be thought of as the real resolution of the spectrograph. The dependence of the FWHM with the wavelength can be mapped when measuring lamp's spectral lines across the spectral range of the instrument.

The following linear relations between the FWHM of the instrumental profile, and the central wavelength of the line (λ_c), were used in the study at hand, determined by Bragança et al. (2012):

- If 3250Å $< \lambda_c <$ 5000Å (`MIKE`, blue side):

$$FWHM_{\text{instr}} = 1.91 \times 10^{-5} \times \lambda_c + 0.047 \tag{2.10}$$

[3]Resolving power is often called "resolution"

- If 5000Å $\leq \lambda_c <$ 9500Å (`MIKE`, red side):

$$FWHM_{\text{instr}} = 3.40 \times 10^{-5} \times \lambda_c - 0.017 \tag{2.11}$$

- `FEROS` spectrograph:

$$FWHM_c = 2.095 \times 10^{-5} \times \lambda_c - 0.001 \tag{2.12}$$

These relations are illustrated on Figure 2.5. The resolution is lower for the longer wavelengths.

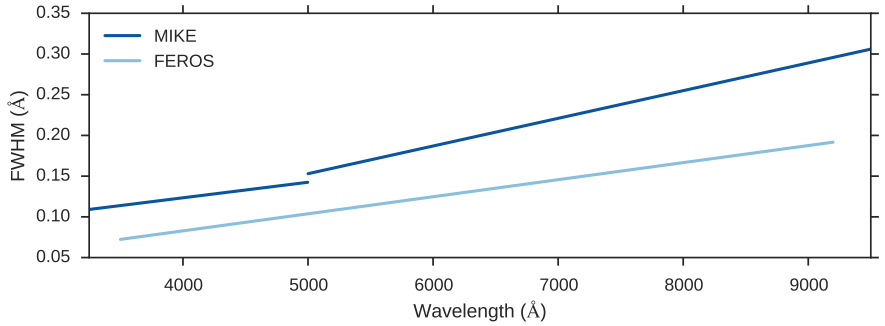

Figure 2.5: Instrumental profiles of `MIKE` and `FEROS` spectrographs

Chapter 3

Stellar sample

3.1 Observations

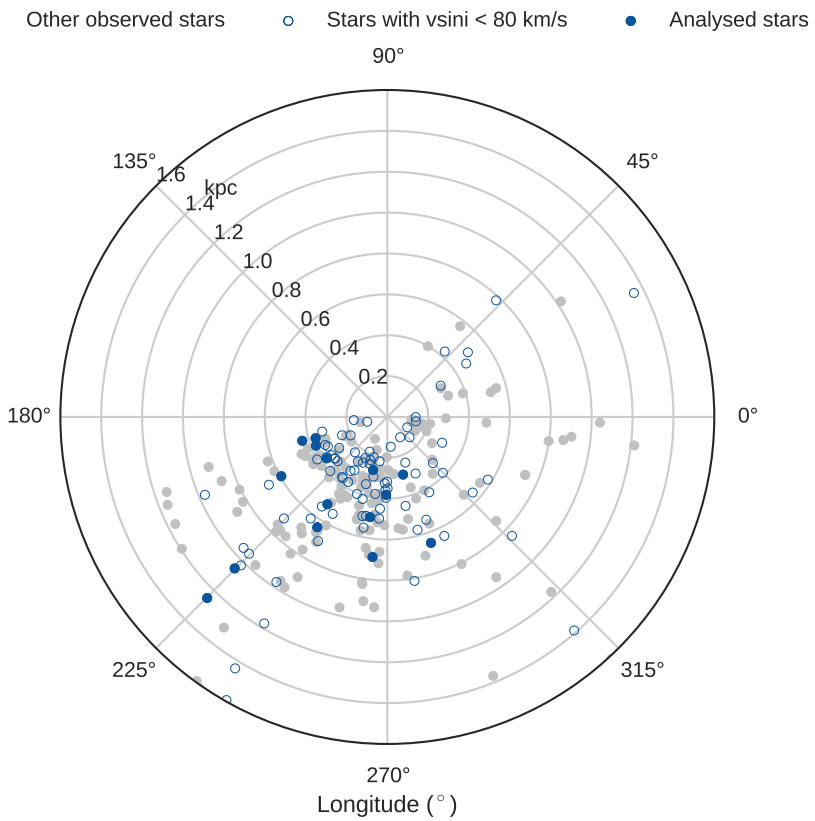

Figure 3.1: Projected postions of the sample stars (distances are from TGAS and Hipparcos catalogues).

The spectra of 379 O9 to B4 main-sequence stars, selected from the Hipparcos catalog (van Leeuwen 2007), were observed in January 8, 9 and April 8, 2007 with the `MIKE` spectrograph at the Magellan Clay 6.5 m telescope on Las Campanas observatory in Chile. `MIKE` is a double

echelle spectrograph – it reflects light into the blue and the red side of the spectrograph in one exposure, each arm equipped with its own shutter and CCD. The spectrograph has a wide wavelength coverage: 3350–5000 Å for the blue side and 4900–9500 Å for the red side. The resolving power for the blue spectra is about R $\sim$ 55000 and 40000 for the red spectra, taken with 0.7 arc second slit width (Bernstein et al. 2003). The stars in the sample are all nearby and relatively bright (V $\sim$ 5–10). Figure 3.1 shows projected positions of these stars, with Sun in the center and zero longitude pointing towards the Galactic centre. Exposure times ranged from a few seconds to a few minutes, and the signal-to-noise ratios are of the order of 100.

The methodology for determining the stellar parameters and elemental abundances for the stars (described in the next chapter), was tested with three stars HIP37036, HIP38164 and HIP42828. These stars have published stellar parameters and elemental abundances from the study by Nieva & Przybilla (2012). HIP37036, HIP38164 and HIP42828 were observed on the 30. December 2008, with the ESO/MPI 2.2 m telescope, equipped with the `FEROS` spectrograph.

3.2 Low-rotational velocity sample

The study by Bragança et al. (2012) determined $v \sin i$, spectral type and the effective temperature for 350 stars from the observed sample stars. They found that the majority of theses stars have very high rotational velocities (up to 400 km s^{-1}). As discussed in Section 2.4, the high $v \sin i$ can broaden the spectral lines until they cannot be distinguished from the continuum. This makes precise spectral analysis impossible. The Master's thesis at hand studied a low-rotational velocity ($<$ 22 km s^{-1}) sub-sample of this dataset, consisting of 17 stars observed in January 2007. These stars are marked with filled blue circles on Figure 3.1. Stars in the observed dataset that have still sufficiently low $v \sin i$ and thus could be analysed with same methods in the future, are marked with empty circles. The rest of the dataset is marked with gray. The positions for the stars were taken from Tycho-Gaia Astrometric Solution (TGAS) database (Gaia Collaboration et al. 2016a) and from the Hipparcos astrometric catalogue (van Leeuwen 2007). Positions from two catalogues were used, because TGAS does not provide positions for stars with G-magnitudes less than about 6 mag, as these stars are too bright for Gaia observations (Lindegren et al. 2016). The spectra provided for this study were already reduced and calibrated, with the exception of continuum normalisation.

Continuum normalisation

Careful continuum normalisation is important for two reasons. Firstly, `MIKE` is an echelle spectrograph and this means, that all spectral regions (orders) have specific shapes (illustrated on Figure 3.2a). Secondly, the synthetic spectrum was normalised. Spectrograph's order shape cannot be mimicked when generating a synthetic spectrum.

As the dataset is large, quick differential normalisation methodology for echelle spectrum, developed by Daflon, Hensberge and Bragança (private communication, 2016), was used. The routines in the normalisation methodology allowed to normalise all spectra taken on one observing night simultaneously, but order-by-order (or one wavelength region at a time).

`IRAF`[1] routines and a `python` script was used for the tasks. The methodology is described step-by-step below.

- The spectra was cut into 20 smaller wavelength regions, where the useful spectral lines were situated (e.g as on Figure 3.2b). Smaller wavelength regions can be normalised more easily than whole orders, as the the shape of the order can be complicated (Figure 3.2a). The specific spectral regions had the same length throughout stars.

- To normalise the spectra all at once, the continuum shape should be reduced to the same count level for all stars. This is not true by default, as the exposure time, the luminosity of the stars, and the distance to the stars vary. To reduce the spectra of stars to the same intensity level, a reference star was used. Reference star was chosen among the observed stars for each observation night: HIP53018 for 8th January and HIP34499 for 9th January. The other spectra, taken on the same night, was divided by the spectrum of a reference star, wavelength region wise. The order shape is reduced for this step, and a simple function for each spectra can be found with `IRAF` task *continuum*. Within this task, spline3 function was used, with order 1 or 2. The found functions were close to a straight line, as seen on Figure 3.2c.

- When spectra was divided by its according function, determined in the last step, all spectra was reduced to the same intensity level as the reference spectrum. As the function did not yet represent the order shape, the spectra had still its initial shape.

- The divided spectra of all stars was combined wavelength region wise to a mean spectrum (Figure 3.2d), using `IRAF` *imcombine* task. This mean spectrum represented the general order shape and a normalisation function was found from it with `IRAF` task *continuum*. The original spectra were not radial velocity corrected, so the specific spectral lines combine to one wide spectral line. Also, the different strengths of spectral lines are averaged. This only affects the shape of the continuum, when the Stark-broadened Balmer lines are combined (these wavelength regions are normalised later separately).

- The spectra of stars, that were reduced to the same intensity level before, was then divided by the normalisation function found from the mean spectrum. The spectra was thus normalised to unity (Figure 3.2e and 3.2f).

Fitting for the order shape can be complicated. The differential normalisation routines make the normalisation of echelle spectra quick, as finding a order profile for a mean spectrum is faster than finding it separately for all stars and orders. This is very beneficial when dealing with tens to hundreds of stars. The quality of normalisation depends mostly on the length of the wavelength region extracted from the orders, and the presence of wide Balmer lines. As the spectral line analysis methodology in this study was based on line-to-line fitting, the correct continuum level around each line was very important. The orders cover about 100–200 Å, but normalising a few tens of Å wavelength regions is easier, as the order shape is then less complex. Balmer lines are so wide in the spectra of B-stars, it can be difficult to estimate where the continuum ends and Balmer line wings start. However, these lines were very important for the stellar parameter estimation, as they are sensitive to surface gravity.

[1] IRAF is distributed by the National Optical Astronomy Observatory, which is operated by the Association of Universities for Research in Astronomy, Inc., under cooperative agreement with the National Science Foundation.

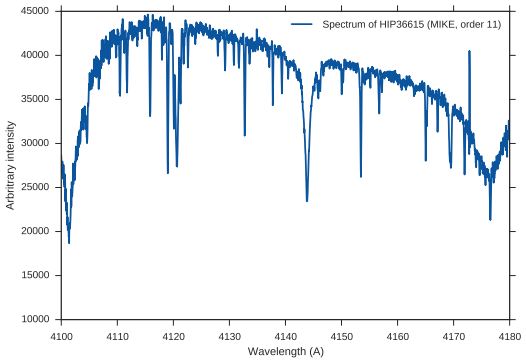

(a) Full order

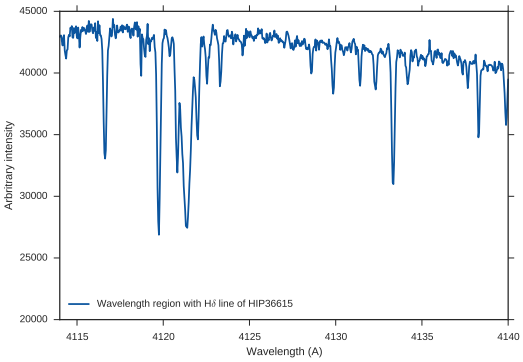

(b) Chosen wavelength region

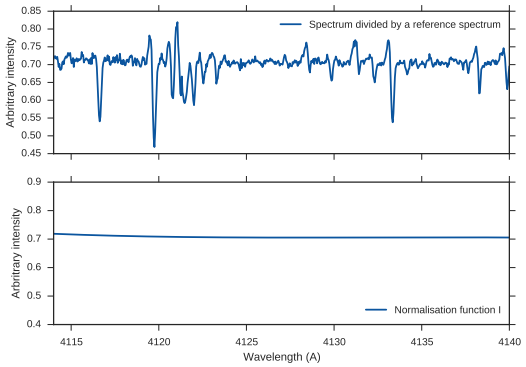

(c) Spectrum divided with the reference spectrum and the resulting continuum function

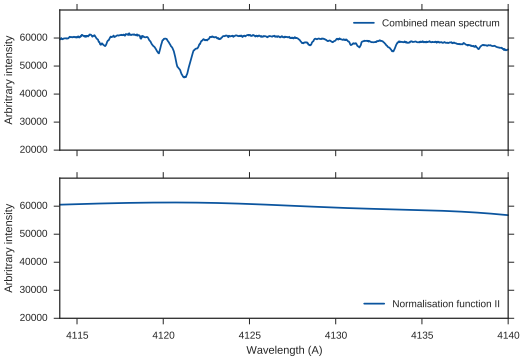

(d) Combined spectrum and the resulting normalisation function.

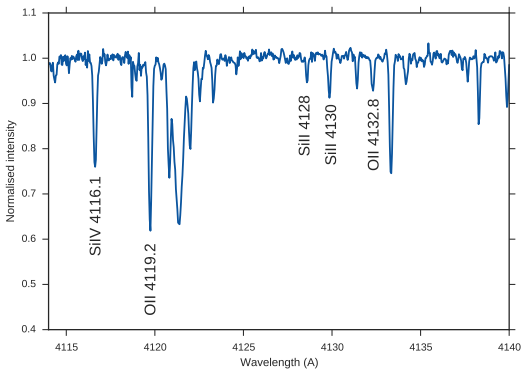

(e) Normalised spectrum

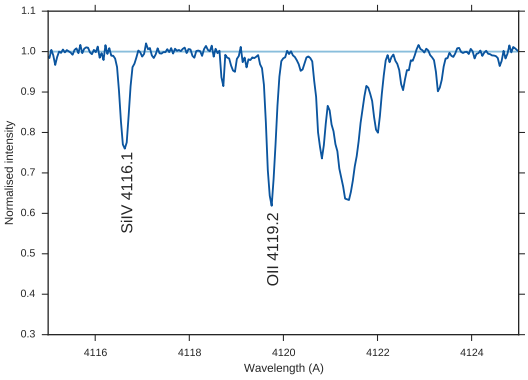

(f) Normalised spectrum, zoomed in

Figure 3.2: Steps in the normalisation routine

For Balmer lines, `IRAF` task *continuum* alone was used, instead of bulk-normalisation routines. During the analysis process later, a scale parameter was used to shift the continuum level of the synthetic spectrum upwards or downwards to fit the normalised continuum level of the observed spectrum perfectly.

Chapter 4

Methodology

The observed spectrum was compared with a synthetic spectrum, based on model atmospheres and model atoms, to analyse the shapes of spectral lines. Line-by-line χ^2-fitting process of silicon, oxygen and hydrogen lines was used with statistical methods for quantifying effective temperature, projected rotational velocity, micro- and macroturbulence, surface gravity, Si and O abundance. Although all the stellar parameters and elemental abundances should be determined simultaneously, it is computationally difficult to keep many parameters free when fitting a line. An iterative methodology was used instead, narrowing in on the best fitting set of stellar parameters with each iteration. In the following sections, this methodology is described in detail, as well as input models and initial parameter values are presented.

4.1 Model atomospheres

This study uses a grid of NLTE model atmospheres (described in Chapter 2.3), calculated using the `TLUSTY` code (Hubeny & Lanz 1995). The grid covers 20 values of effective temperature and with 13 values of surface gravity. The temperature ranges from 14000 K up to 33000 K, in steps of 1000 K. Surface gravity varies from 3 dex to 4.5 dex in steps of 0.12 dex. The models were calculated with microturbulent velocity of 2 km s^{-1} and for six chemical compositions. The stellar parameters can acquire other values than determined by a certain model atmosphere, by interpolating between the model atmospheres in the grid when calculating the synthetic spectrum. Although all model atmospheres were calculated with a fixed microturbulent velocity, this spectral line widening parameter can be changed when calculating the synthetic spectrum.

4.2 Atomic data

Model atoms were compiled by Daflon and Bragança (private communication, 2016) from various sources: model atoms for hydrogen, helium, nitrogen, and sulphur are published in the `TLUSTY` homepage[1]; neon model atom has been updated by Cunha et al. (2006); models for carbon, oxygen, and silicon have been updated by Daflon (private communication, 2016).

[1] http://nova.astro.umd.edu/Tlusty2002/tlusty-frames-data.html

Correction of the log gf values

The $\log gf$ values and photoionization cross-sections were taken from `TOPbase` online atomic database[2]. $\log gf$ is a combination of the statistical weight of the lower level (g) and the oscillator strength (f) which is related to the atomic transition probability. Calculated $\log gf$ values are often less reliable, than the laboratorial or astrophysical values, as there are many simplifications and assumptions made to make quantum mechanical calculations for complex atoms computable. The $\log gf$ value has a strong effect on the abundance determination. In the weak line approximation (valid for lines that are not close to saturation), the strength of the spectral line can be described by the following equation (Gray 2005, p. 389)

$$\log \frac{W_\lambda}{\lambda} = \log C + \log A + \log gf - \theta_{\rm ex}\chi + \log \lambda - \log \kappa_c \tag{4.1}$$

Here, the $\log C$ describes the stellar parameters, $\log A$ is the abundance of the element, $\theta_{\rm ex}\chi$ is the excitation temperature ($\theta_{\rm ex} = 5040/T$) and the excitation potential for the lower level, $\log \lambda$ is the wavelength and $\log \kappa_c$ is the continuum absorption. The uncertainties in $\log gf$ calculation translate directly to errors in abundance determination.

While receiving the first abundance results from the sample stars, a large scatter in line-to-line abundances was noticed. This large scatter was systematic in respect to different stars and could not be reduced by fine-tuning the stellar parameters for each star. This scatter was mainly caused by the uncertainties of the $\log gf$ values, but perhaps also from other systematic errors in model atoms and model atmospheres. Using benchmark stars, with known stellar parameters and elemental abundances, astrophysical $\log gf$ values can be determined using Equation 4.1.

Table 4.1: Stellar parameters, Si and O abundances for three benchmark stars (Nieva & Przybilla 2012)

star	$T_{\rm eff}$ (K)	$v \sin i$ (km s^{-1})	ζ (km s^{-1})	$\log g$ (dex)	ξ (km s^{-1})	A(Si)[3] (dex)	$\sigma_{A(\rm Si)}$ (dex)	A(O) (dex)	$\sigma_{A(\rm O)}$ (dex)
HIP42828	22900	11	20	3.6	5	7.52	0.12	8.79	0.08
HIP38164	31500	29	37	3.95	8	7.49	0.12	8.79	0.01
HIP37036	26300	14	20	4.15	3	7.53	0.06	8.76	0.09

This study used three stars: HIP37036, HIP38164 and HIP42828, studied previously by Nieva & Przybilla (2012), as benchmark stars. Table 4.1 presents the effective temperature ($T_{\rm eff}$, projected rotational velocity ($v \sin i$), macroturbulent velocity (ζ), surface gravity ($\log g$), microturbulent velocity (ξ), Si and O abundances of the benchmark stars. For each star, the silicon and oxygen abundance values were found through the methodology (discussed later in the Chapter), using the stellar parameters from Nieva & Przybilla (2012). Then, the abundance value determined from a specific line was compared with the "real" abundance value of the element of the star (from Nieva & Przybilla (2012)). The difference in the abundance values (ΔA) can be interpreted as the difference between the "real" $\log gf$ value and the

[2] http://cdsweb.u-strasbg.fr/topbase/topbase.html

[3] notation $A(X) = \varepsilon(X) = log(nX/nH) + 12$ is used throughout this thesis

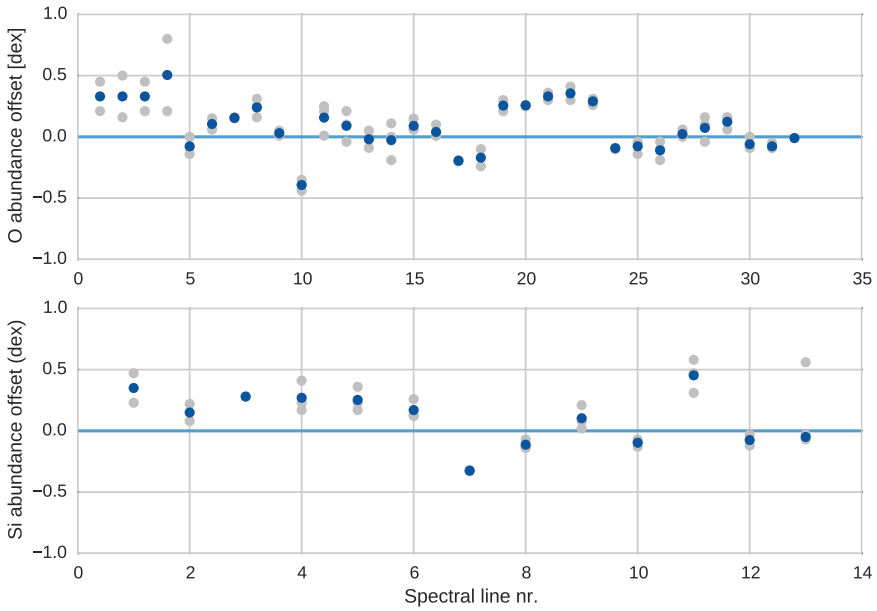

Figure 4.1: The line-by-line differences between the abundance determined using TOPbase $\log gf$ values, and the abundance from Nieva & Przybilla (2012) study, averaged over three benchmark stars (blue markers), and for the benchmark stars separately (gray markers). For better illustration, each spectral line is represented by a number, rather than its wavelength (see Table B.1 and Table B.2 in Appendix B for specific silicon and oxygen lines).

calculated value. Following Equation 4.1:

$$\log A_{\text{real}} \propto -\log gf_{(TOP)} - \Delta\text{A} \tag{4.2}$$

When finding ΔA for the same line transition, but for the three calibration stars, a systematic offset was seen – ΔA was similar for the three stars. This is illustrated on Figure 4.1, where the offset (gray markers) is averaged over the two/three stars for each line (blue markers). The zero line represents the "real" abundance, which corresponds to the silicon and oxygen abundances of the calibration stars (different values for the three stars). The abundance determined from a spectral line using the `TOPbase` $\log gf$ values, differed from the expected abundance value even up to 0.5 dex. The `TOPbase` $\log gf$ values were turned into astrophysical $\log gf$ values using this averaged ΔA, following the Equation 4.2. Appendix B lists all $\log gf$ corrections and shows the spectral lines from the three benchmark stars. For some spectral lines, only two stars could be used to average ΔA. Blends and lines that were not seen in the spectra of the benchmark stars did not get corrections. Blending might result in a contaminated abundance value and in wrong astrophysical $\log gf$ value, due to the dependence on the atomic parameters of multiple spectral lines.

The benchmark stars were then re-analysed with the new $\log gf$ values, so acquiring new stellar parameters and elemental abundances for these three stars. The comparison with the literature values will be presented and discussed in Section 4.5. The $\log gf$ corrections

greatly reduced the line-to-line scatter in abundance determination, as well as allowed better stellar parameter determination. This is illustrated in Appendix C, where stellar parameter determination for HIP34499 is shown. This star has the lowest silicon abundance, so it was an interesting case to test the $\log gf$ correction on. Two cases are presented: stellar parameter estimation with `TOPbase` $\log gf$ values and the corrected values. $\log g$ estimation from Balmer lines is not shown, as only the $\log gf$ for Si and O lines were corrected. All stellar parameters, except microturbulence velocity, had better estimations with the corrections. Microturbulence was underestimated with the new $\log gf$ values, but this was accounted for with the more conservative assigned error.

4.3 Stellar parameter determination

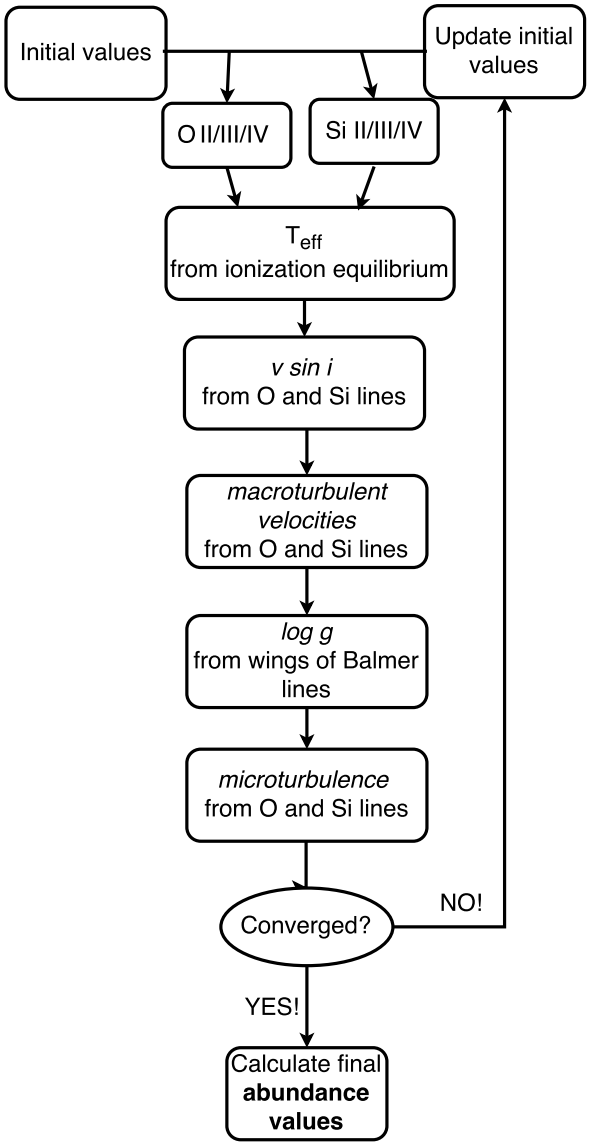

Figure 4.2: Iterative methodology used to find the stellar parameters and elemental abundances

The steps taken to determine stellar parameters and elemental abundances are shown on Figure 4.2. The methodology is based on routines described by Bragança et al. (2015); Hunter et al. (2005). Synthetic spectra was generated with the `SYNSPEC` software (Hubeny & Lanz 1995), which is a program for calculating the spectrum emergent from a given model atmosphere, complemented by the program `ROTINS`, which calculates the rotational and instrumental convolutions for the spectrum produced by `SYNSPEC`. It is tied together by the graphical interface `SYNPLOT`, which allows to perform interactive work with `SYNSPEC` and `ROTINS`. On top of it all, `ipython` packages and scripts have been developed by Bragança et al. (2015), to

use with `SYNPLOT`, to accommodate the methodology. For each star in the analysis procedure, an `ipython` script is created, that uses `SYNPLOT` and follows the methodology, with selected silicon and oxygen lines. In the next Sections, details of the methodology are discussed.

Initial values

The methodology needs initial values for all the stellar parameters and elemental abundances to start the analysing process. The initial values should be reasonably close to the true value (e.g typical values for the B spectral type stars) for the methodology to work. Bragança et al. (2012) study on the same sample, determining photometric effective temperatures and rotational velocities from He I lines, provided initial values for $T_{\rm eff}$ and $v \sin i$. Solar values were used for the initial elemental abundances from Asplund et al. (2009); macroturbulence was initially set to a semi-arbitrary value of 7 km s^{-1}, microturbulence to 0 km s^{-1} and surface gravity to 4.0 dex. In B-type stars, macroturbulence varies from star to star 0–40 km s^{-1} (Nieva & Przybilla 2012). Microturbulence values should be around 0–4 km s^{-1} (Nieva & Przybilla 2010a) for main sequence B-star, or up to 8 km s^{-1} (Nieva & Przybilla 2012). Careful selection of the initial parameters leads to fewer iterations necessary to derive the stellar parameters. See Section 4.6, for the comparison between the initial $T_{\rm eff}$ and $v \sin i$ values, and the values from this study.

Effective temperature

The ionization equilibrium of silicon and oxygen were used to determine the effective temperature of the star. For each Si and O spectral line, a synthetic spectrum was calculated, with other stellar parameters kept fixed, for three temperatures, initial temperature and initial temperature ± 1000 K, with elemental abundance left as a free parameter. Ionization equilibrium means that different ionization stages of an element must result in the same abundance value when varying value of effective temperature. Si II/III/IV lines and O I/II/III lines were used to find the ionization equilibrium. An example of silicon ionization equilibrium estimation for HIP36615 is shown on Figure 4.3.

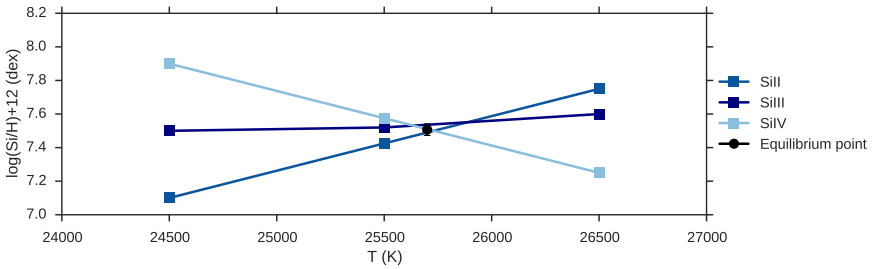

Figure 4.3: Example of the ionization equilibrium of silicon of sample star HIP36615

The equilibrium point for an element was determined by first finding the median and the median absolute deviation of abundances for each ion (so called ionic abundances) of the element, for all temperature values on the $T_{\rm initial} \pm 1000$ K scale. Then, obtaining the weighed

mean and the weighted standard deviation of the ionic abundances, with the weights being the number of spectral lines in that ionization stage. Finally, the equilibrium point was defined as the point where the weighted standard deviation of the ionic abundances was minimum.

The weighed mean of the temperature from oxygen and silicon ionization equilibrium was taken as the true effective temperature, with the weight being the number of ionization stages in oxygen and in silicon respectively. The dispersion around the two ionization equilibrium was representing the error in the effective temperature. This error should be used with caution – the dispersion for some of the stars was below 100 K, which is an unrealistic estimation of a temperature uncertainty of a hot star, although it does show how well the temperature estimates from two elements match. A more likely uncertainty is about 500 K (e.g Simón-Díaz 2010), chosen between the 1% uncertainty from the estimated $T_{\rm eff}$ of Nieva & Przybilla (2012), who used more independent estimators for temperature than this study, and 1000 K uncertainty of Hunter et al. (2005), who used only silicon ionization equilibrium. The temperatures of the sample stars can vary from about 15000 K to over 30000 K, so the number and the strength of silicon and oxygen lines vary from star to star. In some cases, oxygen could not be used in determining the effective temperature, as only one of three ionization stages was available. It was suggested by Nieva & Przybilla (2010b) to change the ionization equilibrium elements according to temperature range of the star, switching between He I/II, C II/III/IV, O I/II, Ne I/II, Si II/III/IV and Fe II/III, but these changes were beyond the scope of the current thesis work. For the lowest temperature star, HIP14898, one ionization stage of both Si and O was available. In this case, the photometric temperature from Bragança et al. (2012) was used. The uncertainties of the photometric temperatures were estimated to be around 2500 K (Bragança et al. 2012). In Chapter 4.6, the photometric and spectroscopic temperatures will be compared and uncertainties in the photometric effective temperatures discussed further.

Projected rotational velocity

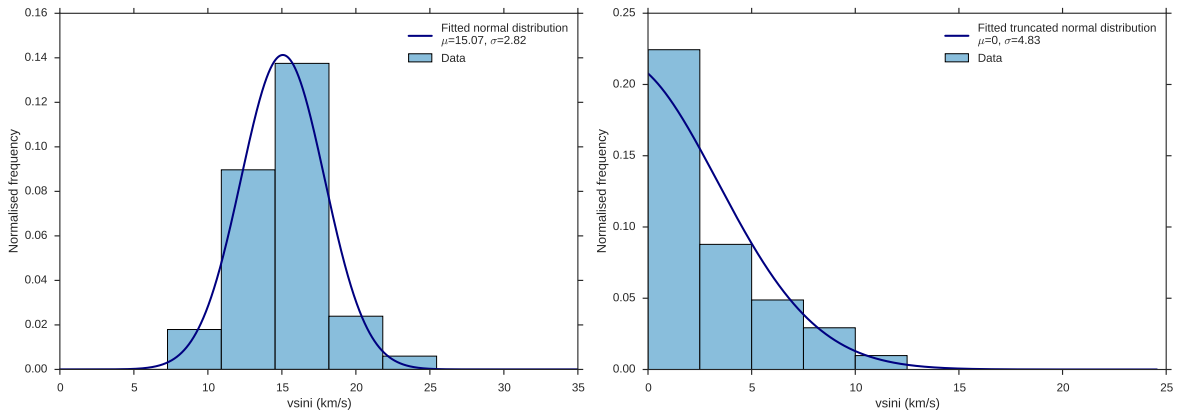

(a) $v \sin i$ for HIP42828 (b) $v \sin i$ for HIP36615

Figure 4.4: Frequencies of projected rotational velocity values from silicon and oxygen line fit for two sample stars.

Although projected rotational velocities were already determined for this sample by Bragança et al. (2012), this parameter has been re-analysed, together with other stellar parameters, in a consistent way. All useful silicon and oxygen lines were fitted by a synthetic spectra, keeping the $v \sin i$ as a free parameter. The best-fitting $v \sin i$ from those lines were expected to follow normal distribution with a mean value and standard deviation, as illustrated on as in Figure 4.4a. As the low rotational sample has some stars with $v \sin i = 0$, the truncated normal distribution was used near zero value (Figure 4.4b). It is suggested to use strong, well defined oxygen and silicon lines for this task (Hunter et al. 2005). The methodology in this study used all lines chosen for the analysis for a certain star. Only the weakest (below 5% of the intensity) and strong blends were discarded. This introduced a larger scatter in the line broadening determination, but also gave a statistical advantage, and allowed to determine the Doppler broadening for stars, which did not show any strong, well defined oxygen and silicon lines.

Macroturbulent velocity

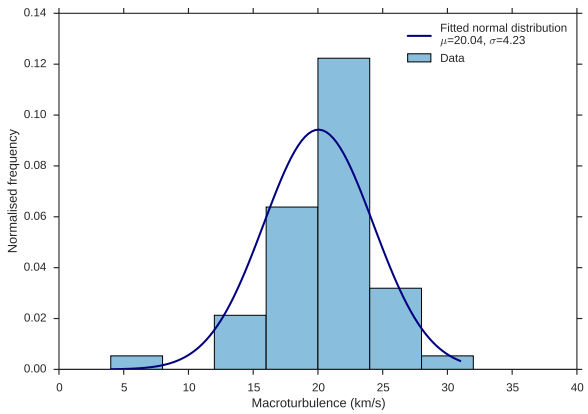

Figure 4.5: Histogram of macroturbulent velocity values from silicon and oxygen line fit for the calibration star HIP42828

Rotational velocity and macroturbulent velocity are both Doppler broadening parameters, but with different broadening profile, so they should be treated separately. The macroturbulent velocity was determined similarly to $v \sin i$, by finding the best fitting macroturbulence values for all useful silicon and oxygen lines, and expecting a normal distribution of these values. This is illustrated on Figure 4.5, with the macroturbulence velocity value distribution for HIP42828. The mean of the distribution defines the macroturbulent velocity for the star. As described in Chapter 2, macroturbulent velocity is described by a Gaussian, and the rotational velocity with an elliptical profile. The shapes of the wings of the metal spectral lines distinguish between these two widening parameters. However, when there are no strong, well defined oxygen and silicon lines, distinction between the two is difficult.

Surface gravity

Balmer α, β, γ and δ line wings were fitted for $\log g$ value, keeping other atmospheric parameters fixed. Because hydrogen lines in the spectrum of B type stars are very wide, the wings may have other spectral lines superposed. To get a clear sample, wavelength region windows were defined by visual inspection, where other spectral lines did not contaminate the fitting process. The mean of the $\log g$ values from different Balmer lines was taken as the $\log g$ value for the star, with standard error describing the uncertainty. For some stars, Hα showed systematically higher $\log g$ values. When this value was higher than one sigma of the surface gravity estimation for all four lines, Hα estimation was discarded.

Microturbulent velocity

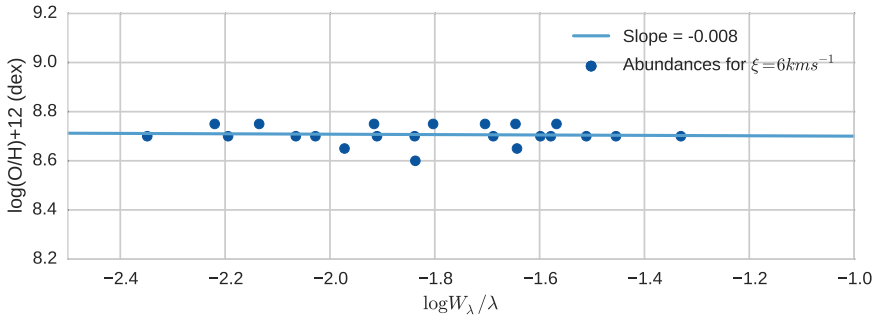

Figure 4.6: Example of microturbulent estimation for oxygen in HIP42828

Spectral lines of the same element should result in the same abundance value, but can have different equivalent widths, as can be understood from Equation 4.1. Microturbulence velocity introduces a slope (a) to the combined Equation 4.1 for all lines of the same species:

$$\log \frac{W_\lambda}{\lambda} \propto a \cdot \log A \tag{4.3}$$

For each line, a synthetic spectrum was calculated for five microturbulence values, with other stellar parameters fixed, and the abundance value as a free parameter. When arranging all analysed lines of one ion on a $\log \frac{W_\lambda}{\lambda}$ vs. $\log A$ plots for these different microturbulent velocity values, the linear relation should have a slope a of zero, as illustrated on Figure 4.6. This was true at a certain microturbulence value, which was determined by interpolation between the slopes determined for the five microturbulence value steps. In essence, the dependence of the estimated abundance on the line strength was eliminated with correct microturbulence value. This method relies on analysing spectral lines that vary in equivalent widths – from weak to intermediate strengths. This methodology made use of Si III and O II lines for this. In lower temperature B stars, the microturbulence was estimated from Si II and O I lines, because the higher ionization stages only showed weak spectral lines. The microturbulence for a star was defined as the mean of the Si and O estimates, with standard deviation describing the uncertainty. Weak lines alone are not sensitive to microturbulence. This is why, for some stars, microturbulece could not be determined, as only weak and insensitive lines were present. Then a microturbulence value $\xi = 0$ km s^{-1} was used, with more conservative 3 km s^{-1} as

the uncertainty. This uncertainty was also used when the slope could not be fully reduced (close to $\xi = 0$ km s^{-1} value), due to an uneven scatter in abundances.

Elemental abundances

If the iterative methodology (Figure 4.2) yielded a converged set of stellar parameters, elemental abundances were determined. The parameters were considered converged, when all previous methodology steps resulted in a well determined stellar parameters peak value, and when none of the stellar parameters changed during a re-iteration. The number of iterations depended on individual star, but was usually between 5–10, with each iteration lasting about 3–7 hours (depending on the number of used spectral lines). Then, the spectral lines were fitted for an abundance value. Figure 4.7 illustrates the line-by-line abundance values for silicon and oxygen for HIP36615. The median with the median absolute deviation described the abundance value for that star. Additionally, random errors were estimated, as described in Section 4.4. Analysing B spectral type stars is a time consuming process – finding stellar parameters and elemental abundances for one star took from a few days to a week using this methodology.

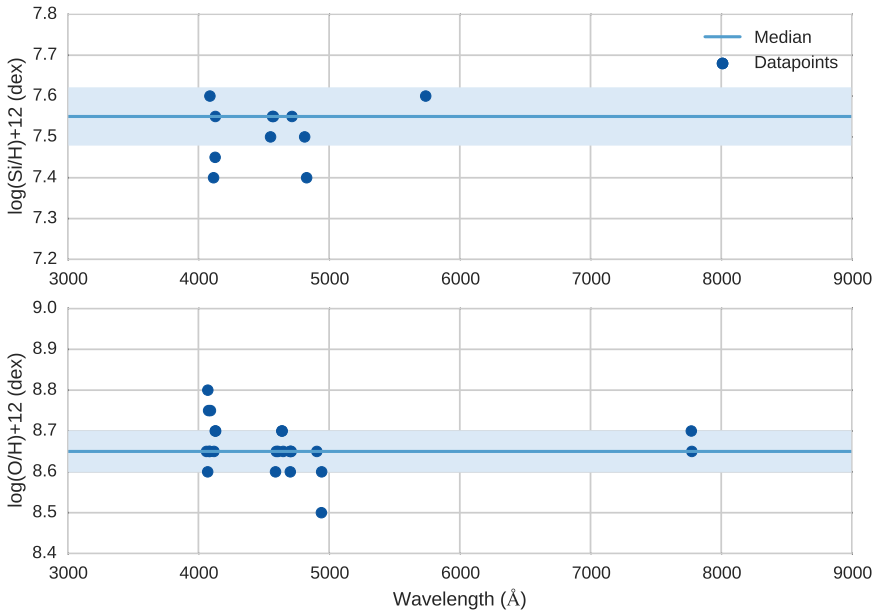

Figure 4.7: Line-by-line abundances of Si and O for sample star HIP36615

Improvements in the methodology

The methodology was developed by Hunter et al. (2005), further improved and written into an `ipython` package by Bragança et al. (2015). Furthermore, the author of this Master's thesis contributed in improving and developing this methodology by:

- adding Hδ line to the $\log g$ estimation (in addition to Hα, Hβ, Hγ lines). This allows for more accurate estimation of the surface gravity, specially when sigma-clipping the Hα line out of the analysis.

- correcting the microturbulence estimator, by substituting the equivalent width (W_λ) to the reduced equivalent width ($\log \frac{W_\lambda}{\lambda}$) in the methodology. Reduced equivalent width follows the weak line approximation equation (Equation 4.1), while pure equivalent width does not.
- switching the microturbulence estimator for lower temperature B stars from O II to O I lines, and from Si III to Si II lines, where stronger spectral lines were present.
- adding truncated normal distribution option in the projected rotational velocity and macroturbulence velocity estimation. Some stars in the sample do have these stellar parameters close to zero. As there are no negative $v \sin i$ or ζ values, normal distribution fails, but truncated normal distribution fits the peak better.
- including random error estimation. The uncertainties from stellar parameter estimation are usually larger than the statistical uncertainties of the abundance analysis. However, random errors are often neglected or not emphasised enough, and thus leaves an impression of higher precision of abundance analysis that it actually deserves. For example, Nieva & Przybilla (2012) estimated the size of the random errors coming from stellar parameters to be about 0.15 dex at maximum, with the majority being accurate to within better than about 0.10 dex, but from one star in their sample. In the study at hand, all sample stars went through a conservative random error estimation. It is time-consuming, but necessary effort.
- subjecting the $\log gf$ values to an accuracy test, and correcting them using the three benchmark stars, as described in Section 4.2.

4.4 Precision and accuracy of the methodology: systematic and random errors

Stellar parameters represent an intertwined set of information, and the methodology described above tries to de-tangle it. The possible systematic errors in quantitative stellar spectroscopy of hot stars was well described by Przybilla et al. (2006) and Nieva & Przybilla (2010b). In the following Section, the uncertainties in the methodology are listed and addressed.

Effective temperature from ionization equilibrium

Ionization equilibrium is considered a powerful tool, as the equilibrium point of three ionization stages of an element constrains both $\log g$ and $T_{\rm eff}$ simultaneously (Nieva & Przybilla 2010a). However, ionization equilibrium from only two ionization stages is sensitive to microturbulence (see Figure 4.8) and can lead to too-low or too-high temperature. With the correct microturbulence value, it would constrain only a combination of $\log g$ and $T_{\rm eff}$. Many of the stars in the sample have only two ionization stages of silicon or oxygen available. However, this study used Balmer lines to determine $\log g$. An independent $\log g$ estimation made it possible to constrain the correct $T_{\rm eff}$ from two ionization stages of an element. Microturbulence was estimated independently, from equivalent widths of Si and O lines. Additionally, ionization stages of two elements – Si and O – were used. Using multiple estimators and independent methods of other stellar parameters, reduced the risk of faulty temperature estimation.

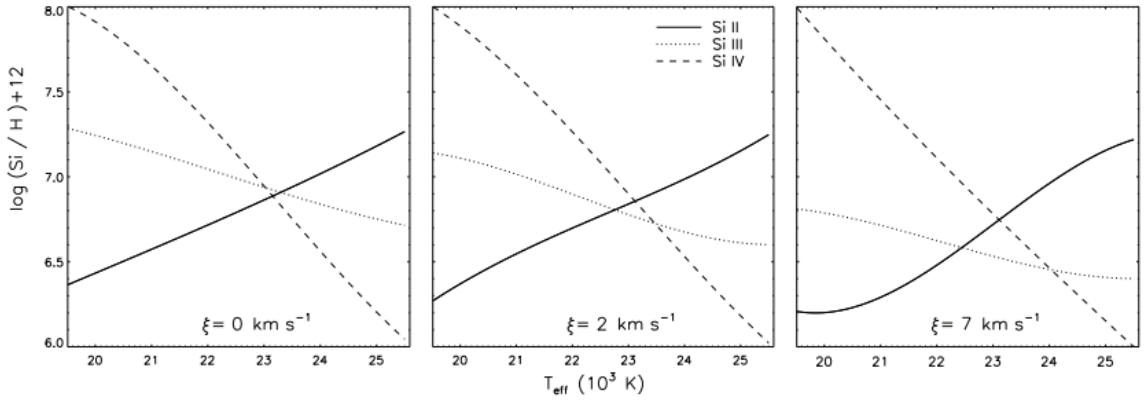

Figure 4.8: Effective temperature determination from silicon ionization equilibrium and the effect of varying microturbulence. The figure is taken from Nieva & Przybilla (2010b).

Surface gravity from Balmer lines

Balmer lines are good indicators for the surface gravity of the stars, due to linear Stark broadening effect. However, they are very sensitive to normalisation errors. Using one Balmer line to estimate $\log g$ is not recommended. Hα, Hβ, Hγ and Hδ were used in the study at hand. For some stars, Hα showed systematically higher $\log g$ values. When this value was higher than one sigma, it was discarded. Hδ line is situated on the edge of a wavelength order of the echelle spectrum, and depending on the width of the line, normalisation can be particularly difficult. The continuum level could not be determined on the blue side of the line. This normalisation error became apparent on visual inspection of the line, during the line-fitting process. Nevertheless, minimum of three Balmer lines were always used to determine best fitting $\log g$.

Microturbulence

Microturbulence needs to be analysed from lines with different equivalent widths. It is beneficial to cross-check the results using multiple elements, as this study did, specially when one of the elements has fewer lines to measure microturbulence from. Ill-chosen microturbulence can affect the effective temperature and surface gravity estimation, as illustrated on Figure 4.8. For low-temperature B-type stars (near 15000 K), microturbulence is estimated from Si II and O I lines instead of Si III and O II, as the later lines are too weak or missing. As mentioned earlier, weak lines alone are not sensitive to microturbulence, and for some stars microturbulece could not be determined. Then a microturbulence value $\xi = 0$ km s^{-1} was used. This decision will be accounted for in the random error estimation, by varying the microtrubulence by 3 km s^{-1}.

Macroturbulence

Macroturbulence estimation is particularly important to slow-rotating objects, as these sample stars are. When not taking into account macroturbulent velocity, the projected rotational

velocities will be overestimated. An example is shown on Figure 4.9, where the pure rotational profile yields $v \sin i = 13.3$ km s^{-1}, but $v \sin i = 0$ km s^{-1} when macroturbulence profile is taken into account. The fit of the line is better with the macroturbulence profile: if the spectral lines are broadened by rotation alone, the line cores are slightly too broad and line wings are insufficiently broad (Przybilla et al. 2006). The line broadening profiles were discussed in Chapter 2.4.

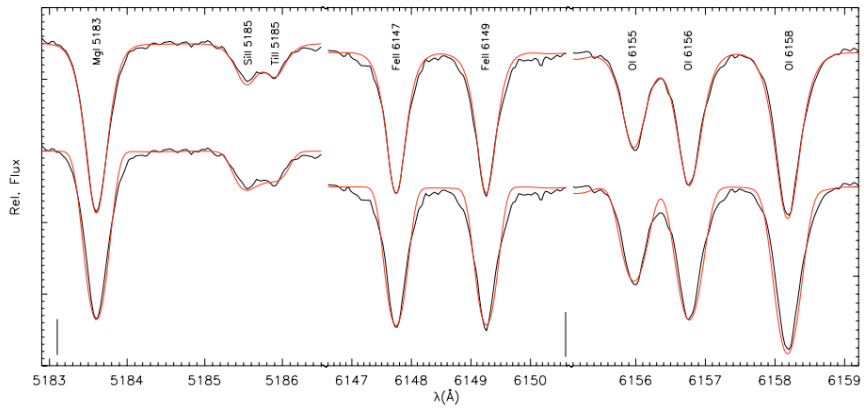

Figure 4.9: Three spectral regions of η Leo. Upper case, observed (black) lines are fitted with synthetic (red) spectrum generated $\zeta = 16.5$ km s^{-1} and zero $v \sin i$. The lower case is made assuming a pure rotational profile with $v \sin i = 13.3$ km s^{-1}. Other stellar parameters are the same. The figure is taken from Przybilla et al. (2006).

When there are no strong, well defined oxygen and silicon lines, distinction between the two Doppler broadening agents can be difficult. In the study at hand, this resulted in a larger deviation around the mean macroturbulence value, which was taken into account in random error estimation. In some previous stellar abundance studies, macroturbulence was neglected (e.g Simón-Díaz 2010), or the lines were fitted for $v \sin i$ and ζ at once with a convolved profile (e.g. Bensby et al. 2003).

Any systematic errors coming from stellar parameter estimations affecting the resulting abundance values, should show on Figures 4.10a and 4.10b as a systematic pattern, but none is seen. Additional systematic errors can come from model atoms and model atmospheres, but are hard to quantify. However, many of these systematic errors are reduced by the astrophysical $\log gf$ corrections.

Random errors from stellar parameter estimation

The methodology estimates stellar parameters and elemental abundances in a consistent way. However, the uncertainties in the stellar parameter estimation do affect the estimation of final elemental abundances. These random errors were estimated by varying stellar parameters by their assigned error (standard deviation), and analysing the difference in the resulting elemental abundances compared to the real elemental abundance ($\Delta_{\varepsilon,\mathrm{param}}$), in following steps:

- varying the stellar parameter by $\pm\sigma_{\mathrm{param}}$ and determining the elemental abundances

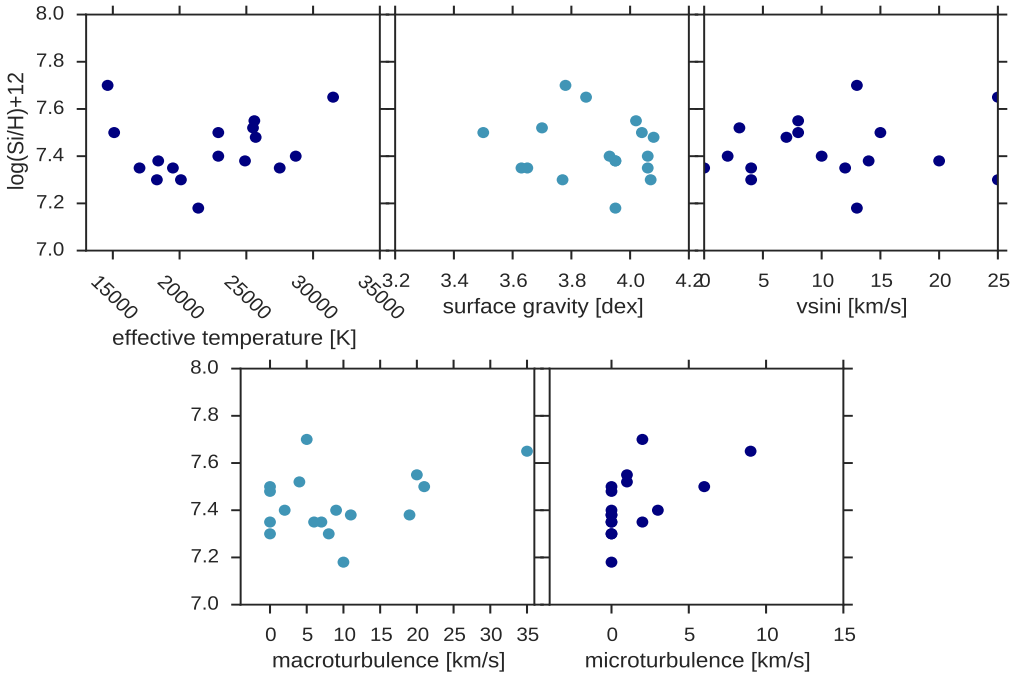

(a) Silicon

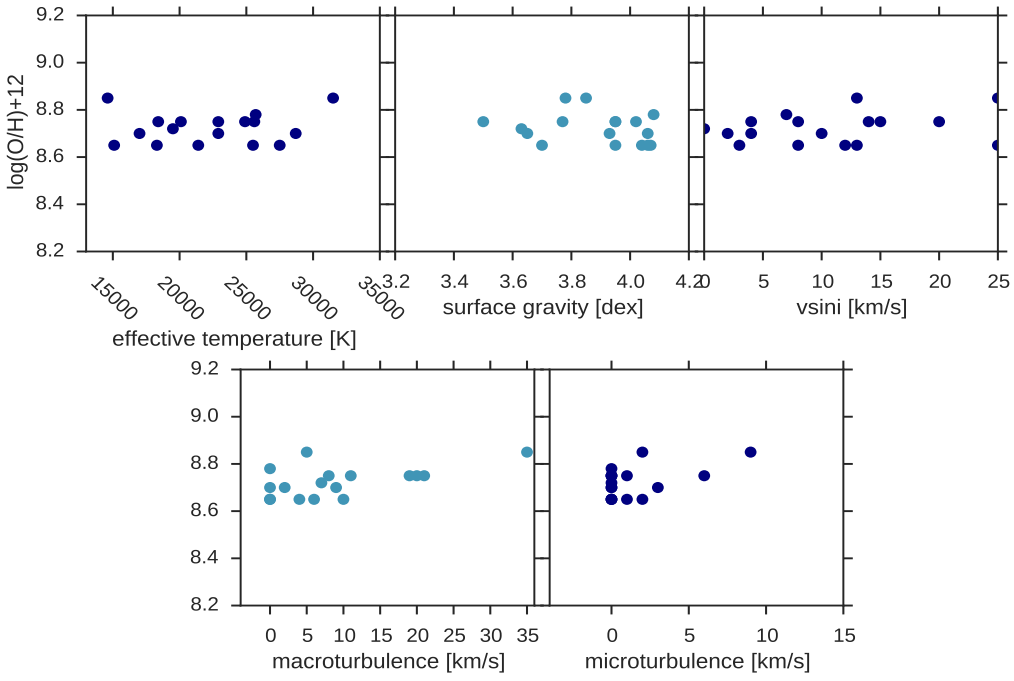

(b) Oxygen

Figure 4.10: Abundance estimation vs. stellar parameters

- calculating the difference between the resulting elemental abundance and the real elemental abundance, $\Delta_{\varepsilon,\mathrm{param}}$
- the maximum $\Delta_{\varepsilon,\mathrm{param}}$ from $\pm\sigma_{\mathrm{param}}$ estimation, was taken as the representative of the random error for that parameter
- $\Delta_{\varepsilon,\mathrm{param}}$ were combined in quadrature:

$$\sigma_{\varepsilon,\mathrm{random}} = \sqrt{\Delta^2_{\varepsilon,\mathrm{Teff}} + \Delta^2_{\varepsilon,\log g} + \Delta^2_{\varepsilon,v\sin i} + \Delta^2_{\varepsilon,\zeta} + \Delta^2_{\varepsilon,\xi}} \tag{4.4}$$

The original σ_{Teff} is the standard deviation of temperature estimations from oxygen and silicon ionization equilibrium, and can be as low as 25 K, when the oxygen and silicon ionization equilibrium gives very close results. The more conservative, and also more realistic uncertainty for the effective temperature is about 500 K. In random error estimation, $\sigma_{\mathrm{Teff}} = 500\ K$ was used when finding the effect of temperature estimation on resulting elemental abundances. If photometric temperature were used (for HIP14898), $\sigma_{\mathrm{Teff}} = 2500\ K$. In normal cases, the standard deviation was used to vary microturbulence. $\sigma_\xi = 3$ km s^{-1} was used to vary microturbulence, when the parameter itself could not be well determined.

Combining these errors in quadrature assumes that the different stellar parameters are independent. This is not so. Stellar parameters are intertwined in a complex manner and varying one parameter not only changes the abundance, but other stellar parameters as well. For example, in B stars hotter temperatures require larger gravities to fit spectra similarly well, but the opposite is true in cooler stars (Schneider et al. 2017). Usually, the covariance of the stellar parameters is ignored, due to the complexity of the relations, and errors are added in quadrature (e.g. Simón-Díaz 2010).

4.5 Common stars with other studies

This study has three stars in common with Nieva & Przybilla (2012) (NP2012) – HIP42828, HIP38164, HIP37036, and one star with Simón-Díaz (2010) and Nieva & Simón-Díaz (2011) (SD2010, NSD2011) – HIP25582. The first three stars were already used as benchmark stars to determine astrophysical $\log gf$ values. Comparing stars with available literature values, provides a good test for the current methodology.

Table 4.2: Testing stellar parameters, Si and O abundances with literature values from Nieva & Przybilla (2012), Simón-Díaz (2010) Nieva & Simón-Díaz (2011)

	HIP	$T_{\rm eff}$ (K)	$v \sin i$ (km s^{-1})	ζ (km s^{-1})	$\log g$ (dex)	ξ (km s^{-1})	A(Si) (dex)	A(O) (dex)
NP2012	42828	22900	11	20	3.60	5	7.52	8.79
		± 300	± 2	± 1	± 0.05	± 1	± 0.12	± 0.08
This work	42828	22900	15	21	3.50	6	7.50	8.75
		± 50	± 3	± 4	± 0.10	± 0	± 0.00 (0.09)	± 0.05 (0.16)
NP2012	38164	31500	29	37	3.95	8	7.49	8.79
		± 300	± 4	± 8	± 0.05	± 1	± 0.12	± 0.10
This work	38164	31500	25	35	3.85	9	7.65	8.85
		±150	± 8	± 7	± 0.09	± 2	± 0.05 (0.22)	± 0.05 (0.13)
NP2012	37036	26300	14	20	4.15	3	7.53	8.76
		± 300	± 2	± 2	± 0.05	± 1	± 0.06	± 0.09
This work	37036	25600	8	20	4.02	1	7.55	8.75
		± 25	± 3	± 3	±0.08	± 0	± 0.05 (0.11)	± 0.05 (0.13)
SD2010	25822	18500	<12	–	4.0	20[4]	7.48	8.79
		± 500	–	–	± 0.10	–	± 0.07 (0.13)	± 0.09 (0.13)
NSD2011	25582	19000	15	8	4.0	2	–	–
		± 300	± 1	± 1	± 0.1	± 1	–	–
This work	25582	18400	14	11	3.95	0	7.38	8.75
		±225	± 2	±4	± 0.05	± 3	± 0.08 (0.16)	± 0.10 (0.19)

The comparison of stellar parameters and elemental abundances are presented in Table 4.2. For the abundances of this work, the dispersion is given, as well as the random error in brackets. NP2012 estimated the random error to be about 0.15 dex and SD2010 0.13 dex. However, the error estimation should not be compared too closely, as different authors view uncertainty estimation differently. Although the stars commons with NP2012 were used to evaluate the true $\log gf$ values (with the elemental abundances and stellar parameters from NP2012), those stars were then re-analysed with the current methodology. One does not expect full agreement between results from different studies as well, as it is very difficult to determine the discrepancies in stellar parameters and elemental abundances of individual stars from different studies. Differences come from quality of the observational material, the methodologies of stellar parameter determination, the choice of spectral lines, the input atomic data, the computer codes and assumptions used for the modelling, etc. As seen from Table 4.2, the afore-described methodology yielded stellar parameters and elemental abundances, that are in good agreement with literature values. The only suspicious result was the effective temperature of HIP37036, that differed by 700 K, when compared to the literature value. However, its uncertainty is only the standard deviation of temperature estimations from oxygen and silicon ionization equilibrium. The more conservative, but also more realistic uncertainty for the effective temperature is more likely to be about 500 K (discussed in Section 4.3). Then, the temperatures from two different studies agree within errorbars. HIP25822 was first studied by SD2010, and then reviewed by NSD2011. However, Nieva & Simón-Díaz (2011) does not give Si and O abundances (but C, N, Ne, Mg, Fe) for individual stars. In conclusion, the methodology used in this study gives agreeable results.

[4]Extra Gaussian-type broadening, to account for the microturbulence and maybe the macroturbulence

4.6 $T_{\rm eff}$ and $v \sin i$ comparison with the initial values

On Figure 4.11, the effective temperature and projected rotational velocities for this work, and the ones determined by (Bragança et al. 2012) are compared. As these stellar parameters were used in initial conditions, the comparison is valuable.

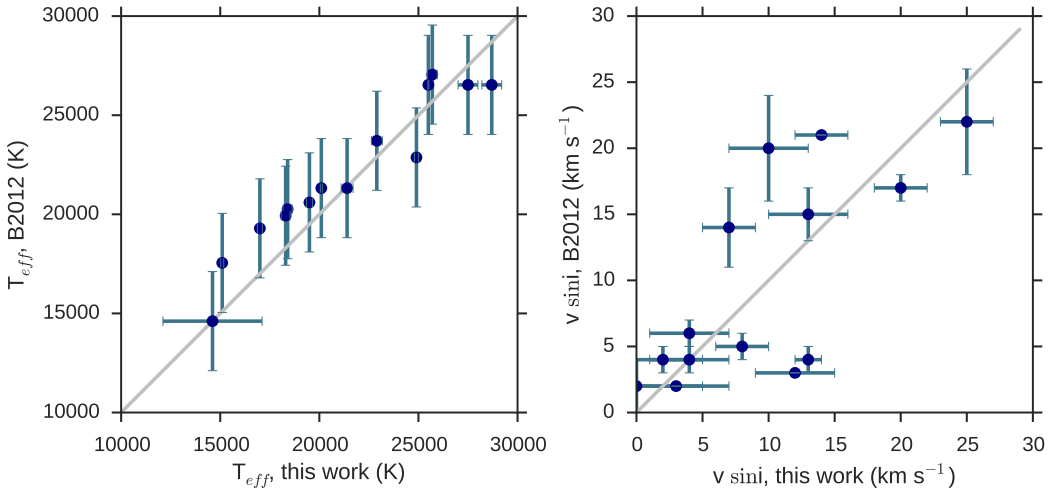

Figure 4.11: Comparison between the $T_{\rm eff}$ and $v \sin i$ derived in this study, and the values derived by Bragança et al. (2012). The solid line represents the locus of equal values.

Effective temperature

The effective temperatures from this study are mostly lower by up to a few 10^3 K, when compared to the photometric effective temperature. This is shown on Figure 4.11, left. Many of the error-bars of temperatures from this study are comparable to the size of the marker. Bragança et al. (2012) determined the photometric (using literature values of U, B and V for each star) temperatures from a calibration of the classical reddening free parameter $Q = (U-B) - X \cdot (B-V)$, where $X = E(U-B)/E(B-V)$:

$$\log T_{\rm eff} = 3.994 - 0.267 \cdot Q + 0.364 \cdot Q^2 \tag{4.5}$$

Although they have not assigned any uncertainties to the temperatures, they admit that: "The estimated $T_{\rm eff}$ values here are good for the purpose of a rough stellar characterization of our sample and, in particular, these suffice for a solid derivation of $v \sin i$ values since the grid of synthetic spectra used here has been computed for steps of 5000 K in $T_{\rm eff}$" (Bragança

et al. 2012). The temperatures differ on average by 1300 K. There seems to be a systematic offset between the temperatures derived with the photometric techniques and the current methodology. The nature of this offset needs more investigation.

Projected rotational velocity

The initial values for $v \sin i$ were determined by Bragança et al. (2012) from measurements of the FWHM of three He I lines at 4026 Å, 4388 Å, and 4471 Å. The measured FWHM was converted to $v \sin i$ by interpolating in the grid of synthetic FWHM of He I lines. However, the macroturbulent velocity was kept as zero in the calculation of the synthetic profiles. When comparing these $v \sin i$ values with the ones from the study at hand, large differences are seen (Figure 4.11, right). There are multiple reasons for this – the methodology in the current study used many metal lines to assess $v \sin i$, took into account micro- and macroturbulence broadening, and assessed all stellar parameters simultaneously in a consistent way. This has to also be kept in mind, when comparing the error-bars from both studies. It can be said, however, that the projected rotational velocity values from Bragança et al. (2012) are still good rough estimates, as the projected rotational velocities in B-type main sequence stars can vary up to 400 km s^{-1}.

Chapter 5

Results & discussion

This Master's thesis aimed to map the present-day silicon and oxygen abundance structure of the Solar neighbourhood. The number of stars, observed for this purpose, is close to 400. However, the stars in the full dataset exhibit large rotational velocities – characteristic, that is common to massive main sequence stars. Thus, this Master's project took under study the lower projected velocity (< 22km s^{-1}) stars in the full dataset. Stellar parameters for these stars have not been determined in a consistent way before, with the exception of photometric effective temperatures and projected rotational velocities (Bragança et al. 2012). The effective temperature, surface gravity, projected rotational velocity, micro- and macroturbulence velocity were found for each star, together with Si and O abundance values. In the following sections, the results for 17 stars are presented, the cosmic abundance standard is reviewed, and the silicon and oxygen abundance values are put onto a spatial map of the Solar neighbourhood.

5.1 Stellar parameters, and Si and O abundances for 17 stars

Table 5.1: Silicon and oxygen abundance values with assigned errors

HIP	A(Si)	$\sigma_{A(\mathrm{Si}),\mathrm{MAD}}$	$\sigma_{A(\mathrm{Si}),\mathrm{r}}$	#	A(O)	$\sigma_{A(\mathrm{O}),\mathrm{MAD}}$	$\sigma_{A(\mathrm{O}),\mathrm{r}}$	#
42828	7.50	0.00	0.09	13	8.75	0.05	0.16	25
38164	7.65	0.05	0.22	7	8.85	0.05	0.13	20
37036	7.55	0.05	0.11	12	8.75	0.05	0.13	30
29417	7.35	0.05	0.18	7	8.78	0.08	0.11	20
36615[1]	7.52	0.07	0.12	11	8.65	0.05	0.07	24
34325	7.35	0.08	0.24	9	8.65	0.05	0.13	22
14898[2]	7.70	0.20	0.54	5	8.85	0.05	0.25	7
50067	7.35	0.10	0.07	9	8.70	0.10	0.11	16
39540[1]	7.40	0.05	0.10	8	8.70	0.05	0.04	26
42357	7.50	0.05	0.19	6	8.65	0.05	0.07	7
33611	7.30	0.10	0.23	7	8.75	0.10	0.08	21
29678	7.48	0.07	0.13	11	8.78	0.03	0.11	32
25582	7.38	0.08	0.16	8	8.75	0.10	0.19	11
39774	7.30	0.05	0.19	5	8.65	0.10	0.15	7
46760	7.40	0.10	0.13	10	8.70	0.10	0.14	26
29127	7.38	0.08	0.06	10	8.75	0.05	0.12	21
34499	7.18	0.07	0.12	8	8.65	0.08	0.17	18

[1] Negative Hipparcos parallax
[2] Photometric temperature

Table 5.1 and Figure 5.1 present the main results of this Master's project – the oxygen and silicon abundances for 17 nearby B-type main sequence stars. In this study, the stellar elemental abundance was defined as the median of the line-by-line abundance values. Uncertainties represent the line-to-line abundance scatter (the median absolute deviation, σ_{MAD}, that is more resilient to outliers), and the random errors coming from stellar parameter estimation (σ_{r}), given separately in the table, but combined in quadrature on the figure. Although both the Table 5.1 and the Figure 5.1 present abundance values for HIP39540 and HIP36615, their position in the Solar neighbourhood was not confirmed (they have negative Hipparcos parallaxes). Figure 5.1 shows the average oxygen and silicon abundances of the Solar neighbourhood from this study (calculated without HIP39540 and HIP36615), and the cosmic abundance standard (CAS) from Nieva & Przybilla (2012). Stellar parameters derived for the stars are presented in Table A.1. Distances in Table A.1 are from van Leeuwen (2007) or TGAS (Gaia Collaboration et al. 2016b) catalogues. The useful Si and O lines, with the determined abundances, for each star are shown in Table D.1.

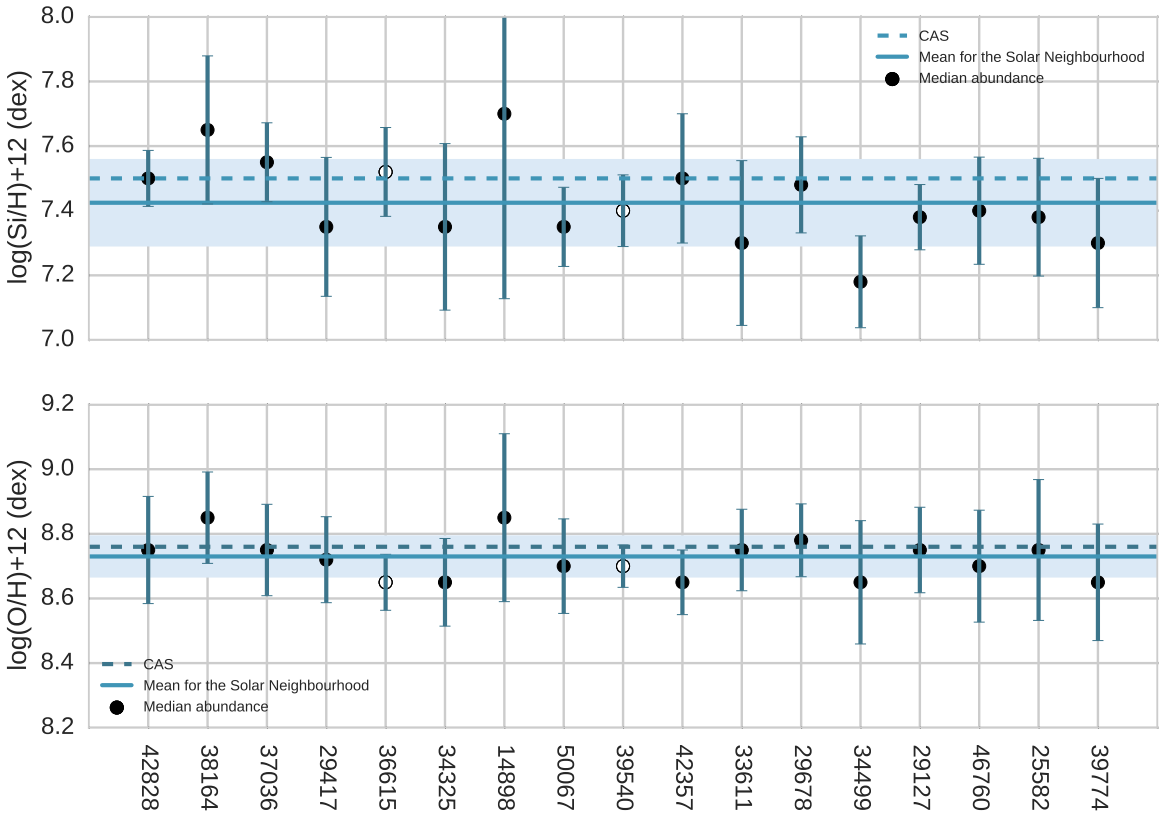

Figure 5.1: Si and O abundances of the stars in the Solar neighbourhood. The error-bar represents the statistical $1\sigma_{\mathrm{MAD}}$ combined with the random error $1\sigma_{\mathrm{r}}$. Mean abundances from this study are compared with the cosmic abundance standard (CAS) from Nieva & Przybilla (2012). Stars without distance estimation are marked with empty symbols.

5.2 Abundance structure of the Solar neighbourhood

Figure 5.2 shows silicon and oxygen abundance for individual stars on a spatial map of the Solar neighbourhood. Note, that the positions of stars are projected onto the zero-latitude plane. As young stars have small velocity dispersion in both radial and height-from-plane direction, the projected distance from Sun on Figure 5.2 is approximately the same as the true distance. Figure 5.2 does not reveal any obvious structural differences in the area, other than the two more distant stars with lower abundances. However, the stellar sample is yet too small to draw conclusions. The mean abundance values of the 1.25 kpc radius Solar neighbourhood are:

- $A(\mathrm{Si}) = 7.42 \pm 0.13$ dex, or 27 ± 10 Si atoms per 10^6 H nuclei
- $A(\mathrm{O}) = 8.73 \pm 0.06$ dex, or 537 ± 85 O atoms per 10^6 H nuclei

The values are computed from median abundances of stars (of equal weights), the uncertainties presented here are the standard deviation of the mean. The silicon abundance has a standard deviation of 0.13 dex, and oxygen 0.06 dex, what translates into 37% and 16% around the

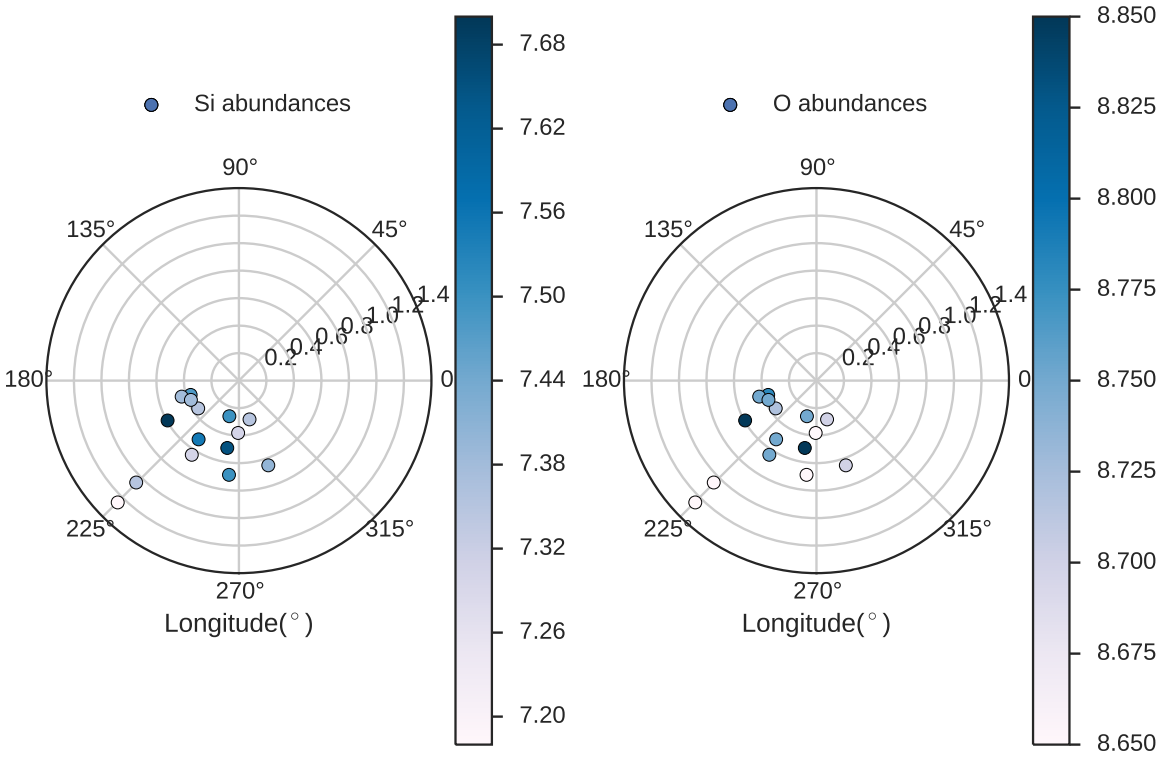

Figure 5.2: Si and O abundance structure in the Solar neighbourhood

mean (of the the absolute abundance values). Due to turbulent mixing of the ISM, via factors like stellar winds, supernova shocks, magnetic fields and density variations of the gas, the ISM is expected to be chemically homogeneous (Nieva & Przybilla 2012). However, the area around the Solar neighbourhood, where these stars are situated (between $180° < l < 315°$, $d < 1.25$ kpc), cannot be considered homogeneous to less than 10% fluctuations from the results of this study. This contradicts the previous findings at first glance. It is important to point out, that previous studies analysed stars, that are closer than 0.5 kpc. 7 stars from the analysed sample are closer than 0.5 kpc. The abundances of these stars vary 16% and 9% for Si and O respectively. Oxygen shows more homogeneity than silicon, but silicon abundances are based on fewer lines, and it are more sensitive to random errors.

5.3 Cosmic abundance standard reviewed

As B-type main sequence stars are good representatives of present-day abundance values in the Milky Way, the derived mean value for the Solar neighbourhood is useful in many ways. It can be used as an abundance standard. The study by Nieva & Przybilla (2012) analysed 29 B-type main sequence stars, from high-resolution and high-S/N `FOCES`, `FEROS` and `ELODIE` observations, to define cosmic abundance standard (CAS), an alternative to Solar abundance standard[1]. It is based on a statistically significant number of stars, instead of one, as with the

[1]CAS was first proposed and defined by Przybilla et al. (2008), with abundances from six stars

Solar standard. Nieva & Przybilla (2012) methodology was similar to the methodology used here: line-profile fitting and an iterative analysis methodology to constrain stellar parameters and elemental abundances simultaneously, although they used more independent indicators for effective temperature and surface gravity. On the other hand, they used a hybrid-LTE approach – LTE model atmospheres and mostly NLTE line formation calculations, in comparison to the superior full-NLTE approach here. The study at hand has confirmed the CAS derived by Nieva & Przybilla (2012) for oxygen and silicon within error-bars. This is illustrated also on Figure 5.1, where the mean of the Solar neighbourhood from this study, and the CAS overlap within uncertainties (the shaded area shows the 1σ of the mean of the Solar neighbourhood).

However, the stars in our sample have on average smaller abundance values and are more heterogeneous, than the stars from Nieva & Przybilla (2012) study. This is revealed more, when (for the sake of consistency) excluding HIP14898, due to the used photometric temperature. Then the resulting average abundances are $A(\mathrm{Si}) = 7.41\pm0.12$ dex and $A(\mathrm{O}) = 8.72\pm0.06$ dex. Additionally, when accounting only the 7 stars in the 0.5 radius around the Sun, the silicon abundance is even lower: $A(\mathrm{Si}) = 7.39\pm0.06$ dex and $A(\mathrm{O}) = 8.73\pm0.04$ dex. The comparison of the common stars in the study (in Chapter 4.5) does not reveal any systematic differences in abundances. Systematic effects coming from stellar parameters, influencing abundances, were not detected (see Figures 4.10b and 4.10a). Either this is an unknown systematic offset from the of the methodology (of either study), or these stars are truly lower in abundances. Differences can arise from the full-NLTE handling, model atoms, or the $\log gf$ calibration of the current study. This offset needs further study. Perhaps the nature of this offset will be revealed when more stars are analysed with the current methodology. Future prospect of this project, started in the frame of this Master's thesis, is to analyse more stars from the full dataset, observed with `MIKE` in 2007, with same analysis methodology, to map the Si, O, and other elements in the Solar neighbourhood further.

5.4 Comparison with other studies

Table 5.2: Present-day oxygen and silicon abundance values in the Solar neighbourhood compared with literature values

Author	A(Si) dex	A(O) dex	Object	radius kpc
This study	7.42 ± 0.13	8.73 ± 0.06	17 B-stars	1.25
NP2012[a]	7.50 ± 0.05	8.76 ± 0.05	29 B-stars	0.5
NSD2011[b]	7.50 ± 0.06	8.77 ± 0.10	13 B-stars in Ori OB1	0.4
SD2010[c]	7.51 ± 0.03	8.73 ± 0.04	13 B-stars in Ori OB1	0.4
M2009[d]	7.20	8.60	150–200 OB stars	1
SDS2011[e]	6.50 ± 0.25 (CEL)	8.52 ± 0.01 (CEL),	HII in Ori OB1	0.4
SDS2011[e]	–	8.65 ± 0.03 (RL)	HII in Ori OB1	0.4
SM2001[f]	7.60 ± 0.14	8.65 ± 0.15	young F & G stars	1.5
C2004[g]& C2006[h]	6.35 ± 0.05	8.54 ± 0.02	ISM	0.8
A2003[i]	–	8.61 ± 0.014	ISM	2.6
S2012[j]	–	8.79 ± 0.12	46 Cepheids	0.5
RDI2011[k]	–	8.52 (CEL), 8.80 (RL)	HII	1.7
RDI2011[k]	–	8.70 (CEL), 8.98 (RL)	PNe	1.7
A2009[l]	7.51 ± 0.03	8.69 ± 0.05	Sun	0

[a] CAS, Nieva & Przybilla (2012);
[b] Nieva & Simón-Díaz (2011), review of SD2010 sample
[c] Simón-Díaz (2010)
[d] Morel (2009), literature review
[e] Simón-Díaz & Stasińska (2011)
CEL – collisionally excited lines, RL – recombination lines
[f] Sofia & Meyer (2001)
[g] Cartledge et al. (2004)
[h] Cartledge et al. (2006)
[i] André et al. (2003)
[j] Stasińska et al. (2012)
[k] Rodríguez & Delgado-Inglada (2011),
[l] Asplund et al. (2009)

The average elemental abundances of the Solar neighbourhood can be compared with present-day values derived from HII regions, the ISM and Cepheids, as well as other types of tracers. Table 5.2 shows results from different studies for different objects. There are a few important points to notice. Firstly, the present-day silicon and oxygen values for the Solar neighbourhood, derived from B-main sequence stars in previous studies (excluding M2009), are in agreement, although different stellar samples are used (with small overlaps). This does point to homogeneity of the Solar neighbourhood. However, the mean silicon abundance from the current study is lower, when compared to the mean values found by Nieva & Przybilla (2012), (Nieva & Przybilla 2010b) and Simón-Díaz (2010), by 0.08, 0.08 and 0.09 dex respectively. For oxygen, the differences are small – 0.03, 0.04 (lower) and 0.00 dex respectively. As men-

tioned earlier, this was not caused by including more distant stars in the dataset, and the cause needs further study. Nevertheless, when accounting the error-bars, the results agree. Therefore, these values are good anchor points for Galactic chemo-dynamical evolution models and when studying large scale Si and O abundance gradients in the Galactic disk. It is important to note, that Table 5.2 shows only results from the latest individual studies with B-type stars. Earlier studies showed a large scatter (up to 0.5 dex) in the derived abundances and indicated lower mean abundances than the Solar values (Stasińska et al. 2012). This was also illustrated in Figure 1.1 in the Introduction of this thesis. Morel (2009) (M2009) collected literature abundance values for 150–200 OB stars in a 1 kpc radius Solar neighbourhood[2]. The reason for the large scatter and suspicious mean abundance, was revealed in the later studies – systematic effects due to a bad determination of the stellar parameters and/or to the assumptions in the abundance analysis. See Morel (2009); Nieva & Przybilla (2010b); Stasińska et al. (2012) for further discussion.

Oxygen abundance derived from local Cepheids agrees with the oxygen abundance from B-type stars, within error-bars. Oxygen abundance derived from B stars is somewhat lower (0.06 dex) than from Cepheids. However, the abundance values derived from Cepheids might be affected by internal mixing, when CNO-material is being dredged up (Luck & Lambert 2011; Stasińska et al. 2012).

The gas-phase abundances in the HII regions and ISM, represent the true present-day situation in the Galaxy. However, elemental abundances of the gas-phase are lower than abundances bound in young stars, because of depletion onto dust grains (Nieva & Przybilla 2012). Additionally, depending on the method used to derive the abundances in them (collisionally excited lines – CEL, or recombination lines – RL), the outcome is very different, as seen from Table 5.2. Simón-Díaz & Stasińska (2011) estimated the amount of oxygen trapped in dust grains for several scenarios of dust formation and found that the oxygen HII region abundance based on recombination lines agrees better with the abundances from B-type stars than the one derived from the collisionally excited lines. The same is seen from the study by Rodríguez & Delgado-Inglada (2011). Hence, the abundance values from HII regions and from diffuse ISM cannot be compared without knowing exact dust depletion mechanisms. However, abundances from B-type stars can provide a depletion-free abundance reference value for dust models.

Young ($<$ 2 Gyr) F and G stars show abundances, that agree within error-bars with the abundances from B-type stars or Cepheids. These stars were considered good present-day abundance represents (Sofia & Meyer 2001). However, these stars can be still older, than the more massive B stars. Assumption that these stars are present-day tracers, relies on age estimation.

8 planetary nebulae (PNe), with ages around 4–6 Gyr, studied by Rodríguez & Delgado-Inglada (2011) show larger abundances than the HII regions of the same study, or B stars of the current study, when analysed through recombination lines. Collisionally excited lines give abundances that agree with the present-day oxygen abundance derived from B stars in

[2]List of collected individual studies concluded are available from: http://www.astro.ulg.ac.be/~morel/liege_colloquium.pdf

the study at hand. PNe and B-star abundances are not really comparable for several reasons. Firstly, similarly to HII regions, PNe have ongoing dust depletion. Secondly, abundances derived from the planetary nebulae can also be affected by internal mixing during the progenitor's evolution. Lastly, PNe are older objects, so the differences in abundances could arise from stellar migration from the inner parts of the Galaxy.

5.5 Comparison with Solar abundances

From Galactic chemical evolution, one would expect the Solar oxygen and silicon abundances to be lower than that in these young objects, as the Sun is a 4.56 Gyr old star. On average in Solar neighbourhood, B stars have 0.09 dex smaller abundance for silicon, and 0.04 dex higher abundance for oxygen, although the differences are within error-bars. Previous studies derived abundances that match with Solar values. If the Sun was formed at the present location, the gas in the vicinity would have been enriched in metal content over the past 4.56 Gyrs as predicted by the chemo-dynamical evolution models for the present Solar vicinity, and the present-day stars would be more metal-rich. The chemical enrichment of the local ISM has been suggested to be small, $\sim$0.1 dex, during this past 4.56 Gyr Chiappini et al. (2003). This would suggest a 7.60 dex silicon abundance, and a 8.80 dex oxygen abundance in the young stars, which is not observed. This disparity indicates, that the Sun has migrated during its lifetime, which is not surprising – Sun has been gaining velocity dispersion during its close encounters with GMC during its lifetime. Newer models (e.g. Minchev et al. 2013) take chemical enrichment and stellar migration into account, and suggest that Sun has migrated from the inner Galactic disk. Minchev et al. (2013) found the most likely birth-place to be between $4.4 < r < 7.7$ kpc, with the highest probability $\sim$5.6 kpc. The inside-out formation model has support from observations – many studies have found present day elemental abundance gradients in the Galactic disk, with abundance values decreasing outwards with radius from the Galactic centre (Daflon & Cunha 2004; Rolleston et al. 2000; Smartt et al. 2001).

5.6 Local chemical abundance values in the context of large scale gradients

The mean abundance values of the Solar vicinity provide necessary boundary conditions for the chemo-dynamical Galaxy evolution models, but they can also be used as a reality-check for the observed large-scale abundance gradients. Abundance gradients are commonly observed in all galaxies, with the metallicities decreasing outward from the galactic centers (Daflon & Cunha 2004). Gradients give vital clues about the evolution of the Milky Way – the disks are believed to form inside-out (Minchev et al. 2013). The present-day abundances derived from observations of tracers at large distances, are more uncertain. The quality of observed spectra goes down with distance, and the distance determination itself is a major problem.

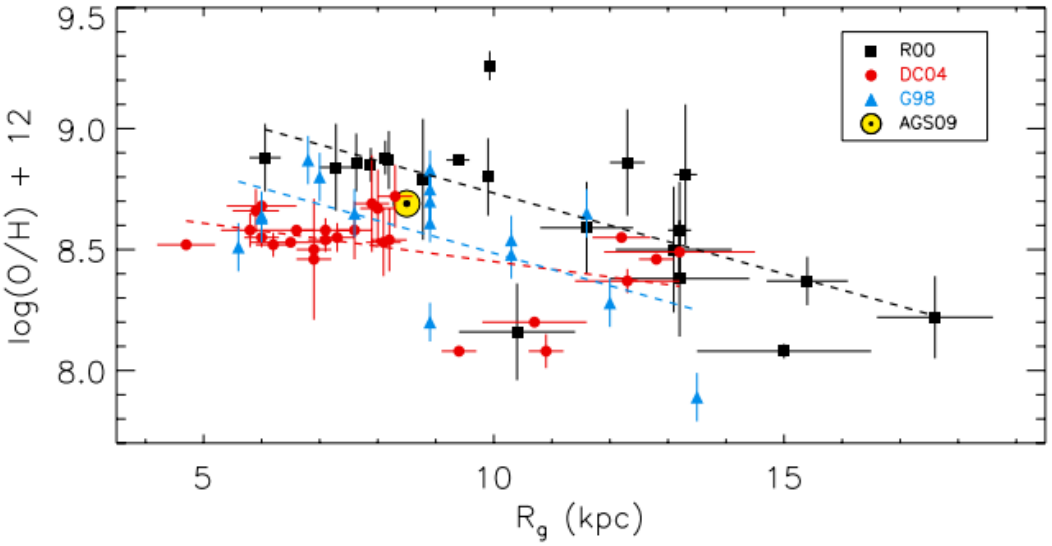

Figure 5.3: Oxygen abundance gradients determined by Daflon & Cunha (2004); Gummersbach et al. (1998); Rolleston et al. (2000) (DC04, G98, R00 respectively) from the analysis of B-type stars. Solar abundance (AGS09) from Asplund et al. (2009). Figure is taken from Stasińska et al. (2012).

The present-day abundance gradients have been determined in numerous studies (Andrievsky et al. 2004; Bragança et al. 2015; Daflon & Cunha 2004; Gummersbach et al. 1998; Rolleston et al. 2000; Smartt et al. 2001), but have stayed rather uncertain, due to non-consistent spectral analysis and small samples. Some examples of the determined gradients are shown on Figure 5.3. There seems to be no consensus between the different determinations (even in the abundance in the Solar neighbourhood). The study by Bragança et al. (in prep.) should bring new views to the matter, from analysing 136 outer disk B stars with the same methodology, than the current Master's thesis (Bragança et al. 2015).

Chapter 6

Conclusions

The story of the formation and evolution of the Milky Way galaxy is written into the chemical and kinematic properties of stars and gas within. Thus, large scale chemical abundance gradients in the Galaxy, small-scale abundance structures, and the mean chemical abundance values in the Solar vicinity, are important constraints to chemical evolution and galaxy formation models. The Master's thesis at hand aimed to map the present-day silicon and oxygen abundance structure of the Solar neighbourhood (extending to 1.5 kpc from the Sun), by determining the stellar atmospheric parameters, and Si and O abundances using high-resolution spectra of B spectral type main sequence stars, observed with the `MIKE` high-resolution spectrograph on the Magellan 6.5-m telescope on Las Campanas in Chile in 2007. While the observed dataset is large, with close to 400 stars, this study analysed only the low-rotational velocity (< 22 km s^{-1}) sub-sample of 17 stars. The current study used line-profile fitting of hydrogen, silicon and oxygen lines, based on grid of NLTE line-blanketed model atmospheres and NLTE line formation calculations. An iterative analysis methodology was used to constrain stellar parameters (effective temperature, surface gravity, projected rotational velocity, micro- and macroturbulent velocity), and silicon and oxygen abundances in a consistent way. The methodology is time-consuming, but rewarding.

The resulting weighed average silicon and oxygen abundance values of the Solar neighbourhood are $A(Si) = 7.42 \pm 0.13$ dex and $A(O) = 8.73 \pm 0.06$ dex. These values agree with the cosmic abundance standard defined by Nieva & Przybilla (2012), within error-bars. However, the stars in our sample have on average smaller abundance values and are more heterogeneous, than the stars from Nieva & Przybilla (2012) study. Silicon abundance is 0.08 dex, and oxygen 0.03 dex lower, than the cosmic abundance standard. The silicon abundance has a deviation of 0.13 dex, and oxygen by 0.06 dex, what translates into 37% and 16% around the mean (of the the absolute abundance values). Nieva & Przybilla (2012) found the Solar neighbourhood, in a 0.5 kpc radius to be chemically homogeneous, with fluctuations less than 10% around the mean. 7 stars of the current study are situated within that radius. The abundances of these stars vary 16% and 9% for Si and O respectively. Mapping the Si and O abundances around the Solar neighbourhood did not reveal any obvious structures.

Although B stars are good present-day Galactic abundance tracers, they are difficult stars to analyse. For example, the wide Balmer lines are good indicators of surface gravity, but they are very sensitive to normalisation problems. Differences between results from independent

studies can arise from the used model atmospheres, model atoms, atomic data, quality of observed spectra, choice of spectral lines, and the overall methodology. In the study at hand, many steps were taken to ensure a realistic view of the abundances in the stars in the Solar vicinity. The $\log gf$ values were put to the test, and were corrected using benchmark stars. The derived Si and O abundances went through a test of systematic uncertainties coming from stellar parameter estimation – none were found. Additionally, thorough and conservative random error estimation was done.

With this Master's thesis, detailed mapping of the present-day Si and O abundances in the Solar neighbourhood has begun. The sample size was arguably small, due to the time-consuming nature of the analysing process. However, the large observational dataset and the tested methodology leaves room for a follow-up study. In the future, other low-rotational velocity sub-sample stars will be analysed, up to a $v \sin i \simeq 80\text{km s}^{-1}$ limit. This would amount to about 100 stars. This, combined with Gaia DR2 positions and chemical abundances for the fast rotating B-type stars in the Solar vicinity (Cazorla et al. 2017), would provide unprecedented view of the present-day Solar neighbourhood, with statistically meaningful cosmic abundance standard and the understanding of the scale of chemical homogeneity in the area.

Acknowledgements

My deepest expression of gratitude goes to Thomas Bensby, for the care he took in supervising this thesis – from giving me the opportunity to work in a project with a scale that goes beyond this thesis, to the detailed reviews of the thesis draft, and everything in between. I most of all appreciate his "door is always open" policy and the long discussions on the nuances of analysing spectra of stars.

This Master's project is part of an international study of B-type main sequence stars near the Solar vicinity, and in the outer Galactic disk. I would like thank the collaborators and advisors – Gustavo Bragança, Simone Daflon, Katia Cunha and Sally Oey, for providing me with the necessary data, giving me a "crash course" in analysing B-stars, and advising me at all times. Among them, special thanks to Gustavo Bragança for guiding me through the more technical aspects of the methodology.

I am grateful for the staff of Lund Observatory for the inspiring and supportive study environment. I am also indebted to the staff of Tartu Observatory in Estonia, for the continuous support.

I would like to thank my parents, Anne and Toomas, for the support and encouragement in my endeavours. Ema ja isa, suur aitäh toetamast ja kaasa elamast!

Last, but not least, I would like to thank my partner Karlis from the bottom of my heart, for the love and support, as well as the patience and advice. Es mīlu tevi!

This Master's thesis was supported by Estonian national scholarship program Kristjan Jaak, which is funded and managed by Archimedes Foundation in collaboration with the Estonian Ministry of Education and Research; as well as by Skype Technologies OÜ and the Information Technology Foundation for Education.

Chapter 7

References

Alves-Brito A., Meléndez J., Asplund M., Ramírez I., Yong D., 2010, Chemical similarities between Galactic bulge and local thick disk red giants: O, Na, Mg, Al, Si, Ca, and Ti, Astron. Astrophys. vol. 513, A35

Anders F., Chiappini C., Rodrigues T.S., Miglio A., Montalbán J., Mosser B., Girardi L., Valentini M., Noels A., Morel T., Johnson J.A., Schultheis M., Baudin F., de Assis Peralta R., Hekker S., Themeßl N., Kallinger T., García R.A., Mathur S., Baglin A., Santiago B.X., Martig M., Minchev I., Steinmetz M., da Costa L.N., Maia M.A.G., Allende Prieto C., Cunha K., Beers T.C., Epstein C., García Pérez A.E., García-Hernández D.A., Harding P., Holtzman J., Majewski S.R., Mészáros S., Nidever D., Pan K., Pinsonneault M., Schiavon R.P., Schneider D.P., Shetrone M.D., Stassun K., Zamora O., Zasowski G., 2017, Galactic archaeology with asteroseismology and spectroscopy: Red giants observed by CoRoT and APOGEE, Astron. Astrophys. vol. 597, A30

André M.K., Oliveira C.M., Howk J.C., Ferlet R., Désert J.M., Hébrard G., Lacour S., Lecavelier des Étangs A., Vidal-Madjar A., Moos H.W., 2003, Oxygen Gas-Phase Abundance Revisited, Astrophys. J. vol. 591, 1000–1012

Andrievsky S.M., Luck R.E., Martin P., Lépine J.R.D., 2004, The Galactic abundance gradient from Cepheids. V. Transition zone between 10 and 11 kpc, Astron. Astrophys. vol. 413, 159–172

Asplund M., Grevesse N., Sauval A.J., Scott P., 2009, The Chemical Composition of the Sun, ARA&Avol. 47, 481–522

Bensby T., Alves-Brito A., Oey M.S., Yong D., Meléndez J., 2011, A First Constraint on the Thick Disk Scale Length: Differential Radial Abundances in K Giants at Galactocentric Radii 4, 8, and 12 kpc, Astrophys. J. vol. 735, L46

Bensby T., Feltzing S., Gould A., Yee J.C., Johnson J.A., Asplund M., Meléndez J., Lucatello S., Howes L.M., McWilliam A., Udalski A., Szymański M.K., Soszyński I., Poleski R., Wyrzykowski Ł., Ulaczyk K., Kozłowski S., Pietrukowicz P., Skowron J., Mróz P., Pawlak M., Abe F., Asakura Y., Bhattacharya A., Bond I.A., Bennett D.P., Hirao Y., Nagakane M., Koshimoto N., Sumi T., Suzuki D., Tristram P.J., 2017, Chemical evolution of the Galactic bulge as traced by microlensed dwarf and subgiant stars. VI. Age and abundance structure of the stellar populations in the central sub-kpc of the Milky Way, ArXiv e-prints

Bensby T., Feltzing S., Lundström I., 2003, Elemental abundance trends in the Galactic thin and thick disks as traced by nearby F and G dwarf stars, Astron. Astrophys. vol. 410, 527–551

Bensby T., Feltzing S., Oey M.S., 2014, Exploring the Milky Way stellar disk. A detailed elemental abundance study of 714 F and G dwarf stars in the solar neighbourhood, Astron. Astrophys. vol. 562, A71

Bergemann M., Ruchti G.R., Serenelli A., Feltzing S., Alves-Brito A., Asplund M., Bensby T., Gruyters P., Heiter U., Hourihane A., Korn A., Lind K., Marino A., Jofre P., Nordlander T., Ryde N., Worley C.C., Gilmore G., Randich S., Ferguson A.M.N., Jeffries R.D., Micela G., Negueruela I., Prusti T., Rix H.W., Vallenari A., Alfaro E.J., Allende Prieto C., Bragaglia A., Koposov S.E., Lanzafame A.C., Pancino E., Recio-Blanco A., Smiljanic R., Walton N., Costado M.T., Franciosini E., Hill V., Lardo C., de Laverny P., Magrini L., Maiorca E., Masseron T., Morbidelli L., Sacco G., Kordopatis G., Tautvaišienė G., 2014, The Gaia-ESO Survey: radial metallicity gradients and age-metallicity relation of stars in the Milky Way disk, Astron. Astrophys. vol. 565, A89

Bernstein R., Shectman S.A., Gunnels S.M., Mochnacki S., Athey A.E., 2003, MIKE: A Double Echelle Spectrograph for the Magellan Telescopes at Las Campanas Observatory, in: Instrument Design and Performance for Optical/Infrared Ground-based Telescopes, eds. Iye M., Moorwood A.F.M., vol. 4841 of Proc. SPIE, 1694–1704

Bragança G.A., Daflon S., Cunha K., Bensby T., Oey M.S., Walth G., 2012, Projected Rotational Velocities and Stellar Characterization of 350 B Stars in the Nearby Galactic Disk, Astronomical Journalvol. 144, 130

Bragança G.A., Lanz T., Daflon S., Cunha K., Garmany C.D., Glaspey J.W., Borges Fernandes M., Oey M.S., Bensby T., Hubeny I., 2015, Non-LTE Abundances in OB stars: Preliminary Results for 5 Stars in the Outer Galactic Disk, in: New Windows on Massive Stars, eds. Meynet G., Georgy C., Groh J., Stee P., vol. 307 of IAU Symposium, 90–91

Carbon D.F., 1979, Model atmospheres for intermediate- and late-type stars, ARA&Avol. 17, 513–549

Carollo D., Beers T.C., Lee Y.S., Chiba M., Norris J.E., Wilhelm R., Sivarani T., Marsteller B., Munn J.A., Bailer-Jones C.A.L., Fiorentin P.R., York D.G., 2007, Two stellar components in the halo of the Milky Way, Naturevol. 450, 1020–1025

Cartledge S.I.B., Lauroesch J.T., Meyer D.M., Sofia U.J., 2004, The Homogeneity of Interstellar Oxygen in the Galactic Disk, Astrophys. J. vol. 613, 1037–1048

Cartledge S.I.B., Lauroesch J.T., Meyer D.M., Sofia U.J., 2006, The Homogeneity of Interstellar Elemental Abundances in the Galactic Disk, Astrophys. J. vol. 641, 327–346

Casagrande L., Silva Aguirre V., Schlesinger K.J., Stello D., Huber D., Serenelli A.M., Schönrich R., Cassisi S., Pietrinferni A., Hodgkin S., Milone A.P., Feltzing S., Asplund M., 2016, Measuring the vertical age structure of the Galactic disc using asteroseismology and SAGA, Mon. Not. R. Astron. Soc. vol. 455, 987–1007

Catanzaro G., 2014, Stellar Atmospheres: Basic Processes and Equations, 9–23

Cazorla C., Morel T., Naze Y., Rauw G., Semaan T., Daflon S., Oey M.S., 2017, Chemical abundances of fast-rotating massive stars. I. Description of the methods and individual results, ArXiv e-prints

Chiappini C., Górny S.K., Stasińska G., Barbuy B., 2009, Abundances in the Galactic bulge: results from planetary nebulae and giant stars, Astron. Astrophys. vol. 494, 591–610

Chiappini C., Matteucci F., Romano D., 2001, Abundance Gradients and the Formation of the Milky Way, Astrophys. J. vol. 554, 1044–1058

Chiappini C., Romano D., Matteucci F., 2003, Oxygen, carbon and nitrogen evolution in galaxies, Mon. Not. R. Astron. Soc. vol. 339, 63–81

Churchwell E., Walmsley C.M., 1975, Are the electron temperatures of H II regions a function of galactic radius, Astron. Astrophys. vol. 38, 451–454

Cunha K., Frinchaboy P.M., Souto D., Thompson B., Zasowski G., Allende Prieto C., Carrera R., Chiappini C., Donor J., Garcia-Hernandez A., Elia Garcia Perez A., Hayden M.R., Holtzman J., Jackson K.M., Johnson J.A., Majewski S.R., Meszaros S., Meyer B., Nidever D.L., O'Connell J., Schiavon R.P., Schultheis M., Shetrone M., Simmons A., Smith V.V., Zamora O., 2016, Chemical abundance gradients from open clusters in the Milky Way disk: results from the APOGEE survey, ArXiv e-prints

Cunha K., Hubeny I., Lanz T., 2006, Neon Abundances in B Stars of the Orion Association: Solving the Solar Model Problem?, Astrophys. J. vol. 647, L143–L146

Daflon S., Cunha K., 2004, Galactic Metallicity Gradients Derived from a Sample of OB Stars, Astrophys. J. vol. 617, 1115–1126

Deharveng L., Peña M., Caplan J., Costero R., 2000, Oxygen and helium abundances in Galactic Hii regions - II. Abundance gradients, Mon. Not. R. Astron. Soc. vol. 311, 329–345

Esteban C., García-Rojas J., Peimbert M., Peimbert A., Ruiz M.T., Rodríguez M., Carigi L., 2005, Carbon and Oxygen Galactic Gradients: Observational Values from H II Region Recombination Lines, Astrophys. J. vol. 618, L95–L98

Fernández-Alvar E., Carigi L., Allende Prieto C., Hayden M.R., Beers T.C., Fernández-Trincado J.G., Meza A., Schultheis M., Santiago B.X., Queiroz A.B., Anders F., da Costa L.N., Chiappini C., 2017, Chemical trends in the Galactic halo from APOGEE data, Mon. Not. R. Astron. Soc. vol. 465, 1586–1600

Gaia Collaboration, Brown A.G.A., Vallenari A., Prusti T., de Bruijne J.H.J., Mignard F., Drimmel R., Babusiaux C., Bailer-Jones C.A.L., Bastian U., et al., 2016a, Gaia Data Release 1. Summary of the astrometric, photometric, and survey properties, Astron. Astrophys. vol. 595, A2

Gaia Collaboration, Brown A.G.A., Vallenari A., Prusti T., de Bruijne J.H.J., Mignard F., Drimmel R., Babusiaux C., Bailer-Jones C.A.L., Bastian U., et al., 2016b, Gaia Data Release 1. Summary of the astrometric, photometric, and survey properties, Astron. Astrophys. vol. 595, A2

Garmany C.D., Glaspey J.W., Bragança G.A., Daflon S., Borges Fernandes M., Oey M.S., Bensby T., Cunha K., 2015, Projected Rotational Velocities of 136 Early B-type Stars in the Outer Galactic Disk, Astronomical Journalvol. 150, 41

Gilmore G., Randich S., Asplund M., Binney J., Bonifacio P., Drew J., Feltzing S., Ferguson A., Jeffries R., Micela G., et al., 2012, The Gaia-ESO Public Spectroscopic Survey, The Messenger vol. 147, 25–31

Gray D.F., 2005, The Observation and Analysis of Stellar Photospheres, 3 edn.

Gummersbach C.A., Kaufer A., Schaefer D.R., Szeifert T., Wolf B., 1998, B stars and the chemical evolution of the Galactic disk, Astron. Astrophys. vol. 338, 881–896

Henry R.B.C., Kwitter K.B., Jaskot A.E., Balick B., Morrison M.A., Milingo J.B., 2010, Abundances of Galactic Anticenter Planetary Nebulae and the Oxygen Abundance Gradient in the Galactic Disk, Astrophys. J. vol. 724, 748–761

Hubeny I., Lanz T., 1995, Non-LTE line-blanketed model atmospheres of hot stars. 1: Hybrid complete linearization/accelerated lambda iteration method, Astrophys. J. vol. 439, 875–904

Hunter I., Dufton P.L., Ryans R.S.I., Lennon D.J., Rolleston W.R.J., Hubeny I., Lanz T., 2005, A non-LTE analysis of the spectra of two narrow lined main sequence stars in the SMC, Astron. Astrophys. vol. 436, 687–695

Kubát J., 2014, Basics of the NLTE Physics, 149–157

Lindegren L., Lammers U., Bastian U., Hernández J., Klioner S., Hobbs D., Bombrun A., Michalik D., Ramos-Lerate M., Butkevich A., Comoretto G., Joliet E., Holl B., Hutton A., Parsons P., Steidelmüller H., Abbas U., Altmann M., Andrei A., Anton S., Bach N., Barache C., Becciani U., Berthier J., Bianchi L., Biermann M., Bouquillon S., Bourda G., Brüsemeister T., Bucciarelli B., Busonero D., Carlucci T., Castañeda J., Charlot P., Clotet M., Crosta M., Davidson M., de Felice F., Drimmel R., Fabricius C., Fienga A., Figueras F., Fraile E., Gai M., Garralda N., Geyer R., González-Vidal J.J., Guerra R., Hambly N.C., Hauser M., Jordan S., Lattanzi M.G., Lenhardt H., Liao S., Löffler W., McMillan P.J., Mignard F., Mora A., Morbidelli R., Portell J., Riva A., Sarasso M., Serraller I., Siddiqui H., Smart R., Spagna A., Stampa U., Steele I., Taris F., Torra J., van Reeven W., Vecchiato A., Zschocke S., de Bruijne J., Gracia G., Raison F., Lister T., Marchant J., Messineo R., Soffel M., Osorio J., de Torres A., O'Mullane W., 2016, Gaia Data Release 1. Astrometry: one billion positions, two million proper motions and parallaxes, Astron. Astrophys. vol. 595, A4

Luck R.E., Lambert D.L., 2011, The Distribution of the Elements in the Galactic Disk. III. A Reconsideration of Cepheids from l = 30deg to 250deg, Astronomical Journalvol. 142, 136

Magic Z., Collet R., Asplund M., Trampedach R., Hayek W., Chiavassa A., Stein R.F., Nordlund Å., 2013, The Stagger-grid: A grid of 3D stellar atmosphere models. I. Methods and general properties, Astron. Astrophys. vol. 557, A26

Majewski S.R., Schiavon R.P., Frinchaboy P.M., Allende Prieto C., Barkhouser R., Bizyaev D., Blank B., Brunner S., Burton A., Carrera R., Chojnowski S.D., Cunha K., Epstein

C., Fitzgerald G., Garcia Perez A.E., Hearty F.R., Henderson C., Holtzman J.A., Johnson J.A., Lam C.R., Lawler J.E., Maseman P., Meszaros S., Nelson M., Coung Nguyen D., Nidever D.L., Pinsonneault M., Shetrone M., Smee S., Smith V.V., Stolberg T., Skrutskie M.F., Walker E., Wilson J.C., Zasowski G., Anders F., Basu S., Beland S., Blanton M.R., Bovy J., Brownstein J.R., Carlberg J., Chaplin W., Chiappini C., Eisenstein D.J., Elsworth Y., Feuillet D., Fleming S.W., Galbraith-Frew J., Garcia R.A., Anibal Garcia-Hernandez D., Gillespie B.A., Girardi L., Gunn J.E., Hasselquist S., Hayden M.R., Hekker S., Ivans I., Kinemuchi K., Klaene M., Mahadevan S., Mathur S., Mosser B., Muna D., Munn J.A., Nichol R.C., O'Connell R.W., Robin A.C., Rocha-Pinto H., Schultheis M., Serenelli A.M., Shane N., Silva Aguirre V., Sobeck J.S., Thompson B., Troup N.W., Weinberg D.H., Zamora O., 2015, The Apache Point Observatory Galactic Evolution Experiment (APOGEE), ArXiv e-prints

Martig M., Fouesneau M., Rix H.W., Ness M., Mészáros S., García-Hernández D.A., Pinsonneault M., Serenelli A., Silva Aguirre V., Zamora O., 2016, Red giant masses and ages derived from carbon and nitrogen abundances, Mon. Not. R. Astron. Soc. vol. 456, 3655–3670

Martín-Hernández N.L., Peeters E., Morisset C., Tielens A.G.G.M., Cox P., Roelfsema P.R., Baluteau J.P., Schaerer D., Mathis J.S., Damour F., Churchwell E., Kessler M.F., 2002, ISO spectroscopy of compact H II regions in the Galaxy. II. Ionization and elemental abundances, Astron. Astrophys. vol. 381, 606–627

McWilliam A., 1997, Abundance Ratios and Galactic Chemical Evolution, ARA&Avol. 35, 503–556

Minchev I., Chiappini C., Martig M., 2013, Chemodynamical evolution of the Milky Way disk. I. The solar vicinity, Astron. Astrophys. vol. 558, A9

Minchev I., Martig M., Streich D., Scannapieco C., de Jong R.S., Steinmetz M., 2015, On the Formation of Galactic Thick Disks, Astrophys. J. vol. 804, L9

Morel T., 2009, Abundances of massive stars: some recent developments, Communications in Asteroseismology vol. 158, 122

Nieva M.F., Przybilla N., 2010a, Atmospheric parameter determination for massive stars via non-LTE spectrum analysis, in: EAS Publications Series, eds. Monier R., Smalley B., Wahlgren G., Stee P., vol. 43 of EAS Publications Series, 167–187

Nieva M.F., Przybilla N., 2010b, Improving Stellar Parameter and Abundance Determinations of Early B-Type Stars, in: Hot and Cool: Bridging Gaps in Massive Star Evolution, eds. Leitherer C., Bennett P.D., Morris P.W., Van Loon J.T., vol. 425 of Astronomical Society of the Pacific Conference Series, 146

Nieva M.F., Przybilla N., 2012, Present-day cosmic abundances. A comprehensive study of nearby early B-type stars and implications for stellar and Galactic evolution and interstellar dust models, Astron. Astrophys. vol. 539, A143

Nieva M.F., Simón-Díaz S., 2011, The chemical composition of the Orion star forming region. III. C, N, Ne, Mg, and Fe abundances in B-type stars revisited, Astron. Astrophys. vol. 532, A2

Oliveira C.M., Hébrard G., 2006, Variations in the D/H Ratio of Extended Sight Lines from Far Ultraviolet Spectroscopic Explorer Observations, Astrophys. J. vol. 653, 345–360

Perryman M.A.C., Lindegren L., Kovalevsky J., Hoeg E., Bastian U., Bernacca P.L., Crézé M., Donati F., Grenon M., Grewing M., van Leeuwen F., van der Marel H., Mignard F., Murray C.A., Le Poole R.S., Schrijver H., Turon C., Arenou F., Froeschlé M., Petersen C.S., 1997, The HIPPARCOS Catalogue, Astron. Astrophys. vol. 323, L49–L52

Portail M., Wegg C., Gerhard O., 2015, Peanuts, brezels and bananas: food for thought on the orbital structure of the Galactic bulge, Mon. Not. R. Astron. Soc. vol. 450, L66–L70

Prialnik D., 2015, An Introduction to the Theory of Stellar Structure and Evolution, 2 edn.

Przybilla N., Butler K., Becker S.R., Kudritzki R.P., 2006, Quantitative spectroscopy of BA-type supergiants, Astron. Astrophys. vol. 445, 1099–1126

Przybilla N., Nieva M.F., Butler K., 2008, A Cosmic Abundance Standard: Chemical Homogeneity of the Solar Neighborhood and the ISM Dust-Phase Composition, Astrophys. J. vol. 688, L103

Przybilla N., Nieva M.F., Butler K., 2011, Testing common classical LTE and NLTE model atmosphere and line-formation codes for quantitative spectroscopy of early-type stars, in: Journal of Physics Conference Series, vol. 328 of Journal of Physics Conference Series, 012015

Rodríguez M., Delgado-Inglada G., 2011, The Oxygen Abundance in the Solar Neighborhood, Astrophys. J. vol. 733, L50

Rolleston W.R.J., Smartt S.J., Dufton P.L., Ryans R.S.I., 2000, The Galactic metallicity gradient, Astron. Astrophys. vol. 363, 537–554

Rudolph A.L., Fich M., Bell G.R., Norsen T., Simpson J.P., Haas M.R., Erickson E.F., 2006, Abundance Gradients in the Galaxy, ApJSvol. 162, 346–374

Ryabchikova T., 2014, Atomic Data: Where to Get Them, How to Use Them, 53–62

Schneider F.R.N., Castro N., Fossati L., Langer N., de Koter A., 2017, BONNSAI: correlated stellar observables in Bayesian methods, Astron. Astrophys. vol. 598, A60

Simón-Díaz S., 2010, The chemical composition of the Orion star forming region. I. Homogeneity of O and Si abundances in B-type stars, Astron. Astrophys. vol. 510, A22

Simón-Díaz S., Stasińska G., 2011, The chemical composition of the Orion star forming region. II. Stars, gas, and dust: the abundance discrepancy conundrum, Astron. Astrophys. vol. 526, A48

Smartt S.J., Venn K.A., Dufton P.L., Lennon D.J., Rolleston W.R.J., Keenan F.P., 2001, Chemical abundances in the inner 5 kpc of the Galactic disk, Astron. Astrophys. vol. 367, 86–105

Sofia U.J., Meyer D.M., 2001, Interstellar Abundance Standards Revisited, Astrophys. J. vol. 554, L221–L224

Spina L., Meléndez J., Karakas A.I., Ramírez I., Monroe T.R., Asplund M., Yong D., 2016, Nucleosynthetic history of elements in the Galactic disk. [X/Fe]-age relations from high-precision spectroscopy, Astron. Astrophys. vol. 593, A125

Stanghellini L., Haywood M., 2010, The Galactic Structure and Chemical Evolution Traced by the Population of Planetary Nebulae, Astrophys. J. vol. 714, 1096–1107

Stasińska G., Prantzos N., Meynet G., Simón-Díaz S., Chiappini C., Dessauges-Zavadsky M., Charbonnel C., Ludwig H.G., Mendoza C., Grevesse N., Arnould M., Barbuy B., Lebreton Y., Decourchelle A., Hill V., Ferrando P., Hébrard G., Durret F., Katsuma M., Zeippen C.J., 2012, Chapter 2 : A Panorama of Oxygen in the Universe, in: EAS Publications Series, eds. Stasińska G., Prantzos N., Meynet G., Simón-Díaz S., Chiappini C., Dessauges-Zavadsky M., Charbonnel C., Ludwig H.G., Mendoza C., Grevesse N., Arnould M., Barbuy B., Lebreton Y., Decourchelle A., Hill V., Ferrando P., Hébrard G., Durret F., Katsuma M., Zeippen C.J., vol. 54 of EAS Publications Series, 65–186

Unsöld A., 1942, Quantitative Analyse des B O-Sternes τ Scorpii. II. Teil: Deutung des Linienspektrums. Kosmische Häufigkeit der leichten Elemente. Elektronendruck P_e, Temperatur T und Schwerebeschleunigung g in der Atmosphäre von τ Scorpii. Mit 8 Abbildungen., ZApvol. 21, 22

van Leeuwen F., 2007, Validation of the new Hipparcos reduction, Astron. Astrophys. vol. 474, 653–664

Wegg C., Gerhard O., Portail M., 2015, The structure of the Milky Way's bar outside the bulge, Mon. Not. R. Astron. Soc. vol. 450, 4050–4069

Appendices

Appendix A

Stellar parameters

Table A.1: Stellar parameter results. Distances (d) and distance errors $d_{\rm err}$ are from Hipparcos or TGAS catalogues.

HIP	d kpc	$e_{\rm d}$ kpc	$T_{\rm eff}$ K	$\sigma_{T_{\rm eff}}$ K	$v \sin i$ km s^{-1}	$\sigma_{v \sin i}$ km s^{-1}	ζ km s^{-1}	σ_ζ km s^{-1}	$\log g$ dex	$\sigma_{\log g}$ dex	ξ km s^{-1}	σ_ξ km s^{-1}
42828	0.24	0.01	22900	50	15	3	21	3	3.50	0.10	6	0
38164	0.51	0.08	31500	150	25	8	35	7	3.85	0.09	9	2
37036	0.52	0.09	25600	25	8	3	20	3	4.02	0.08	1	0
29417	0.37	0.04	19500	225	3	3	6	3	3.74	0.22	0	0
36615	–	–	25500	25	3	4	4	5	3.70	0.12	1	0
34325[1]	1.05	0.53	27500	500	12	3	6	6	4.06	0.18	2	0
14898	1.10	1.68	14610	2500	13	1	5	3	3.78	0.13	2	3
50067	0.29	0.02	17000	125	4	3	0	5	3.65	0.05	0	0
39540	–	–	28700	500	2	3	2	3	4.06	0.11	3	1
42357[1]	0.69	0.20	15100	75	8	2	0	6	4.04	0.17	0	3
33611[1]	0.65	0.23	20100	50	4	3	7	3	3.77	0.03	0	3
29678	0.37	0.07	25700	250	7	2	0	5	4.08	0.08	0	3
39774	0.39	0.05	18300	225	25	2	0	8	4.07	0.03	0	3
46760[1]	0.68	0.15	22900	275	10	3	9	4	3.93	0.06	0	3
29127[1]	0.43	2.0	24900	100	20	2	19	4	3.95	0.09	0	0
25582	0.40	0.11	18400	225	14	2	11	4	3.95	0.05	0	3
34499[1]	1.25	0.79	21400	300	13	3	10	5	3.95	0.04	0	3

[1] TGAS distances

Appendix B

$\log gf$ values, and used Si and O line profiles

Table B.1: Silicon spectral lines and $\log gf$ values. First and second column show the silicon ion and its wavelength. Third and fourth column show the old `TOPbase` and the corrected $\log gf$ values. Fifth and sixt column show the correction and the stars used for the correction. Last column gives the number designeted to the spectral line on Table 4.1 or a comment.

Ion	λ (Å)	$\log gf_{\mathrm{TB}}$ (dex)	$\log gf_{\mathrm{astro}}$ (dex)	ΔA (dex)	stars (HIP)	comment/ Fig. 4.1 nr.
II	4128.05	0.316	0.666	0.350	37036/42828	1
II	4130.89	0.476	0.626	0.150	37036/42828	2
II	5041.02	0.291	0.571	0.280	42828	3
II	5055.98	0.593	-	-	-	blend
II	6347.10	0.297	-	-	-	blend
II	6371.37	-0.003	-	-	-	blend
III	4552.62	0.283	0.553	0.270	37036/42828/38164	4
III	4567.84	0.060	0.313	0.253	37036/42828/38164	5
III	4574.76	-0.418	-0.248	0.170	37036/42828/38164	6
III	4716.65	0.491	0.166	-0.325	37036/42828	7
III	4813.33	0.706	0.593	-0.113	37036/42828/38164	8
III	4819.71	0.823	0.926	0.103	37036/42828/38164	9
III	4828.95	0.938	0.841	-0.097	37036/42828/38164	10
III	5739.73	-0.103	0.350	0.453	37036/42828/38164	11
IV	4088.86	0.200	0.125	-0.075	37036/42828	12
IV	4116.60	-0.110	0.043	0.153	37036/42828/38164	13
IV	4654.31	-0.520/1.220/1.130	-	-	-	several lines

Table B.2: Oxygen spectral lines and log gf values. First and second column show the oxygen ion and its wavelength. Third and fourth column show the old `TOPbase` and the corrected log gf values. Fifth and sixt column show the correction and the stars used for the correction. Last column gives the number designeted to the spectral line on Table 4.1 or a comment.

Ion	λ (Å)	$\log gf_{\mathrm{TB}}$ (dex)	$\log gf_{\mathrm{astro}}$ (dex)	ΔA (dex)	stars (HIP)	comment/ Fig. 4.1 nr.
I	6155.98	-1.120	-	-	-	no lines
I	6156.77	-0.694	-	-	-	no lines
I	6158.18	-0.409	-	-	-	no lines
I	7771.94	0.354	0.684	0.330	37036/42828	1
I	7774.17	0.207	0.537	0.330	37036/42828	2
I	7775.39	-0.015	0.180	0.330	37036/42828	3
I	8446.36	0.231	0.736	0.505	37036/42828	4
I	4062.91	-0.090	-0.167	-0.077	37036/42828/38164	5
II	4071.23	-0.090	0.015	0.105	37036/42828	6
II	4072.15	0.552	0.707	0.155	37036/42828	7
II	4078.84	-0.287	-0.047	0.240	37036/42828/38164	8
II	4083.93	0.150	0.180	0.030	37036/42828	9
II	4085.11	-0.191	-	-	-	blend
II	4087.19	0.532	0.139	-0.393	37036/42828/38164	10
II	4089.29	0.892	-	-	-	blend
II	4092.93	-0.325	-0.168	0.157	37036/42828/38164	11
II	4119.22	0.447	0.537	0.090	37036/42828/38164	12
II	4129.32	-0.945	-0.965	-0.02	37036/42828	13
II	4132.80	-0.945	-0.965	-0.020	37036/42828	14
II	4488.19	-0.440	-	-	-	blend
II	4590.97	0.331	0.421	0.090	37036/42828/38164	15
II	4596.17	0.180	0.220	0.040	37036/42828/38164	16
II	4602.06	0.510	0.315	-0.195	37036/42828	17
II	4609.37	0.670	0.50	-0.170	37036/42828	18
II	4610.17	-0.170	0.085	0.255	37036/42828	19
II	4638.86	-0.325	-0.068	0.257	37036/42828/38164	20
II	4641.81	0.066	0.396	0.330	37036/42828	21
II	4649.14	0.324	0.679	0.355	37036/42828	22
II	4661.63	-0.268	0.022	0.290	37036/42828/38164	23
II	4696.34	-1.380/-0.980	-	-	-	several lines
II	4699.01	0.418	0.325	-0.093	37036/42828/38164	24
II	4701.18	0.088	0.011	-0.077	37036/42828/38164	25
II	4703.16	0.262	0.152	-0.110	37036/42828/38164	26
II	4705.35	0.533	0.556	0.023	37036/42828/38164	27
II	4710.00	-0.090	-0.017	0.073	37036/42828/38164	28
II	4906.83	-0.157	-0.034	0.123	37036/42828/38164	29
II	4941.07	-0.018	-0.078	-0.06	37036/42828/38164	30
II	4943.00	0.307	0.230	-0.077	37036/42828/38164	31
III	5592.25	-0.361	-0.361	0	38164	32

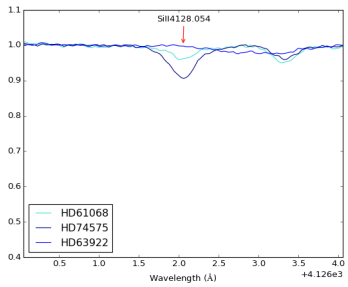
SiII4128.054
HD61068
HD74575
HD63922
Wavelength (Å)
+4.126e3

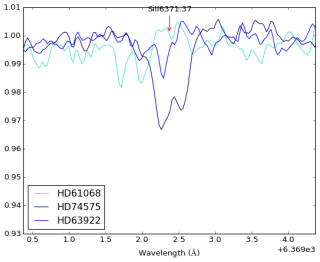
SiII6371.37
HD61068
HD74575
HD63922
Wavelength (Å)
+6.369e3

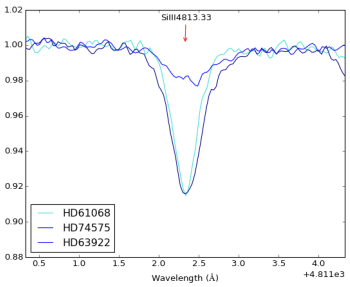
SiIII4813.33
HD61068
HD74575
HD63922
Wavelength (Å)
+4.811e3

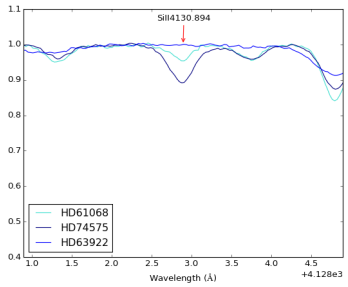
SiII4130.894
HD61068
HD74575
HD63922
Wavelength (Å)
+4.128e3

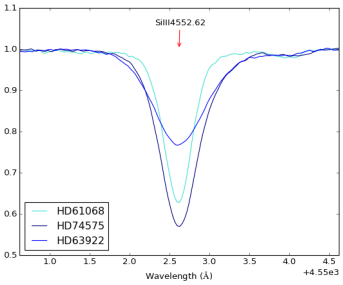
SiIII4552.62
HD61068
HD74575
HD63922
Wavelength (Å)
+4.55e3

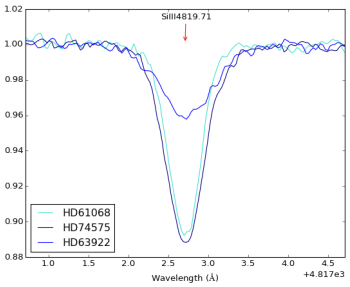
SiIII4819.71
HD61068
HD74575
HD63922
Wavelength (Å)
+4.817e3

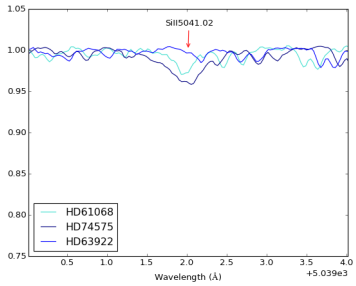
SiII5041.02
HD61068
HD74575
HD63922
Wavelength (Å)
+5.039e3

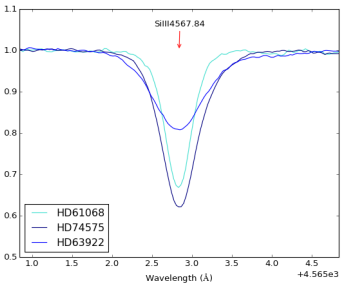
SiIII4567.84
HD61068
HD74575
HD63922
Wavelength (Å)
+4.565e3

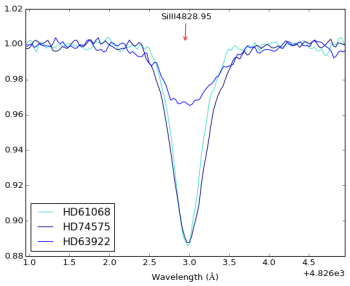
SiIII4828.95
HD61068
HD74575
HD63922
Wavelength (Å)
+4.826e3

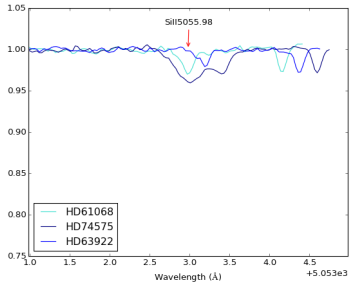
SiII5055.98
HD61068
HD74575
HD63922
Wavelength (Å)
+5.053e3

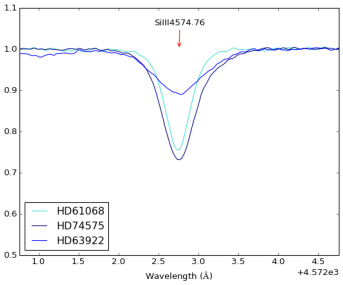
SiIII4574.76
HD61068
HD74575
HD63922
Wavelength (Å)
+4.572e3

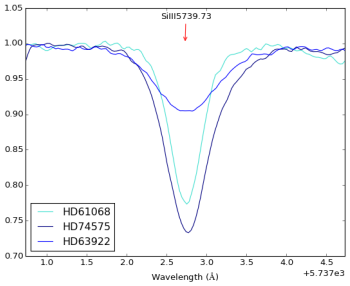
SiIII5739.73
HD61068
HD74575
HD63922
Wavelength (Å)
+5.737e3

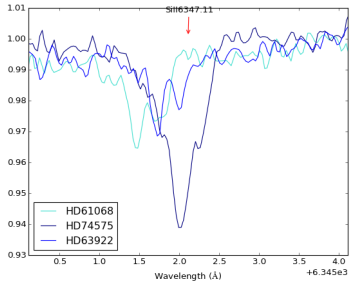
SiII6347.11
HD61068
HD74575
HD63922
Wavelength (Å)
+6.345e3

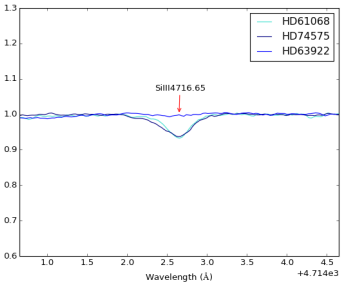
SiIII4716.65
HD61068
HD74575
HD63922
Wavelength (Å)
+4.714e3

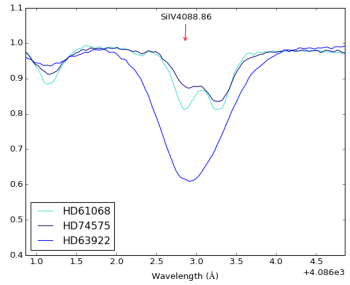
SiIV4088.86
HD61068
HD74575
HD63922
Wavelength (Å)
+4.086e3

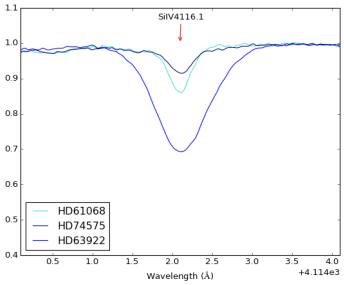
SiIV4116.1
HD61068
HD74575
HD63922
Wavelength (Å)
+4.114e3

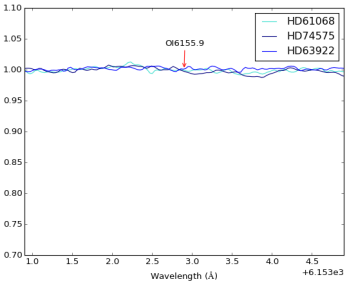
OI6155.9
HD61068
HD74575
HD63922
Wavelength (Å)
+6.153e3

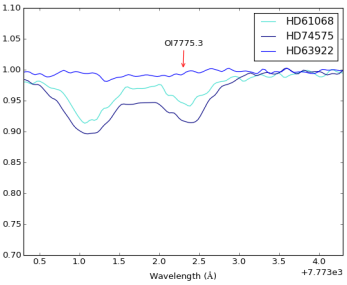
OI7775.3
HD61068
HD74575
HD63922
Wavelength (Å)
+7.773e3

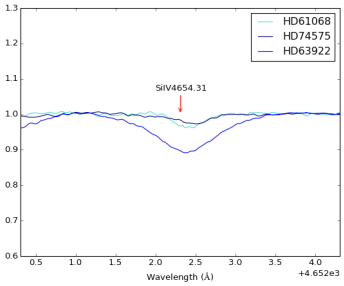
SiIV4654.31
HD61068
HD74575
HD63922
Wavelength (Å)
+4.652e3

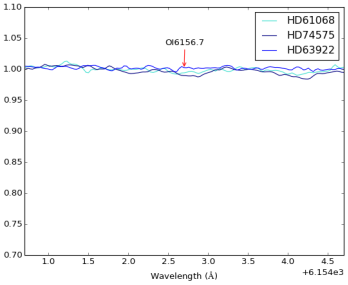
OI6156.7
HD61068
HD74575
HD63922
Wavelength (Å)
+6.154e3

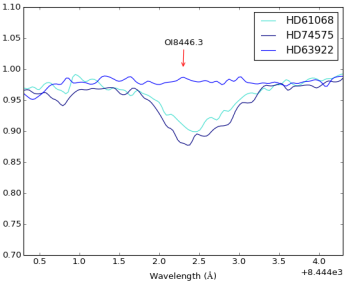
OI8446.3
HD61068
HD74575
HD63922
Wavelength (Å)
+8.444e3

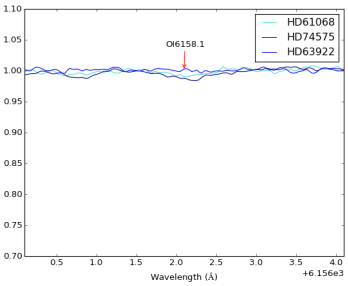
OI6158.1
HD61068
HD74575
HD63922
Wavelength (Å)
+6.156e3

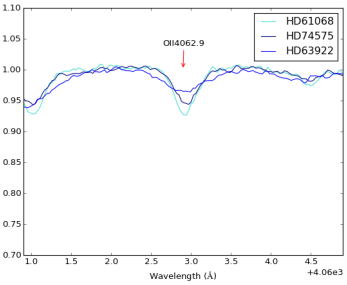
OII4062.9
HD61068
HD74575
HD63922
Wavelength (Å)
+4.06e3

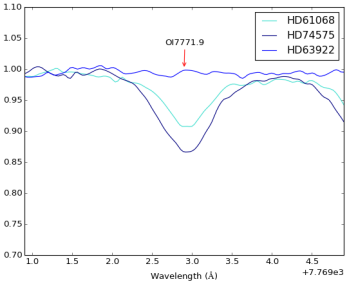
OI7771.9
HD61068
HD74575
HD63922
Wavelength (Å)
+7.769e3

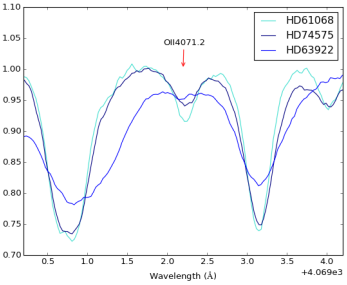
OII4071.2
HD61068
HD74575
HD63922
Wavelength (Å)
+4.069e3

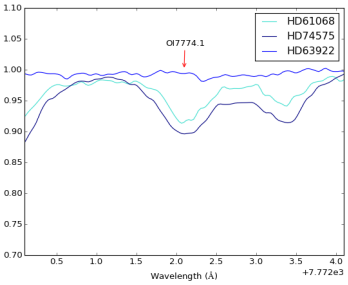
OI7774.1
HD61068
HD74575
HD63922
Wavelength (Å)
+7.772e3

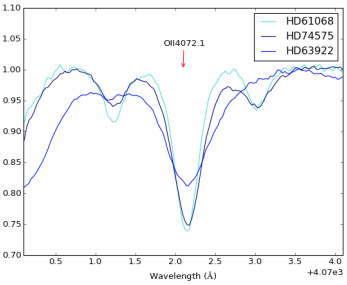
OII4072.1
HD61068
HD74575
HD63922
Wavelength (Å)
+4.07e3

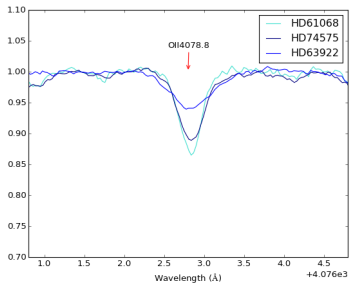
HD61068
HD74575
HD63922
OII4078.8
Wavelength (Å)
+4.076e3

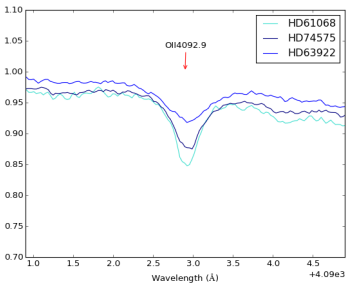
HD61068
HD74575
HD63922
OII4092.9
Wavelength (Å)
+4.09e3

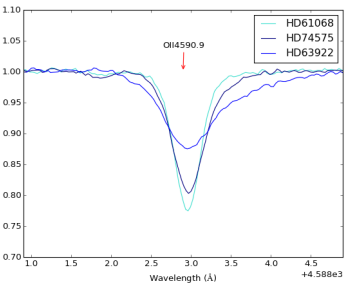
HD61068
HD74575
HD63922
OII4590.9
Wavelength (Å)
+4.588e3

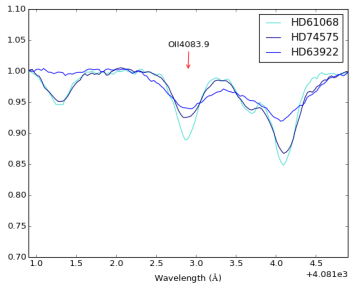
HD61068
HD74575
HD63922
OII4083.9
Wavelength (Å)
+4.081e3

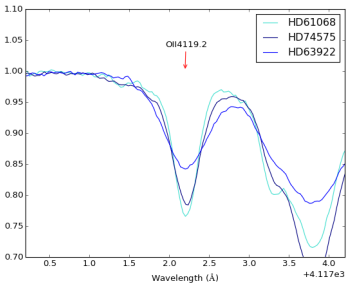
HD61068
HD74575
HD63922
OII4119.2
Wavelength (Å)
+4.117e3

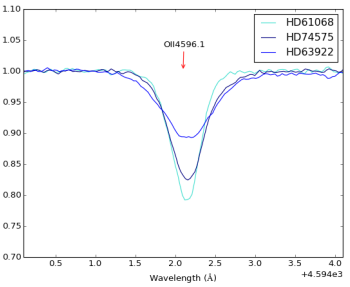
HD61068
HD74575
HD63922
OII4596.1
Wavelength (Å)
+4.594e3

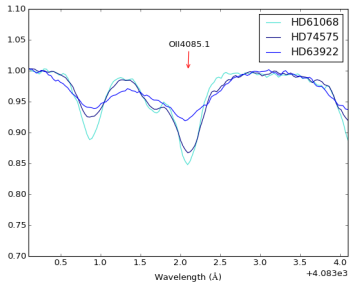
HD61068
HD74575
HD63922
OII4085.1
Wavelength (Å)
+4.083e3

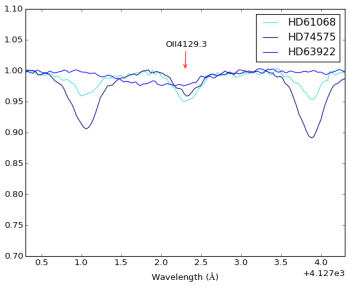
HD61068
HD74575
HD63922
OII4129.3
Wavelength (Å)
+4.127e3

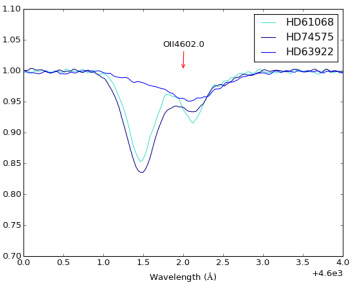
HD61068
HD74575
HD63922
OII4602.0
Wavelength (Å)
+4.6e3

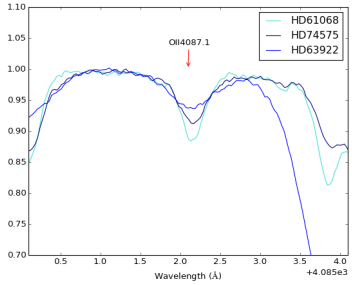
HD61068
HD74575
HD63922
OII4087.1
Wavelength (Å)
+4.085e3

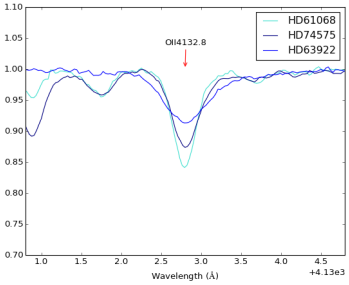
HD61068
HD74575
HD63922
OII4132.8
Wavelength (Å)
+4.13e3

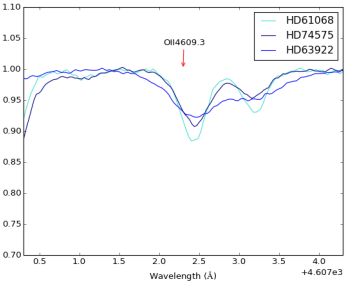
HD61068
HD74575
HD63922
OII4609.3
Wavelength (Å)
+4.607e3

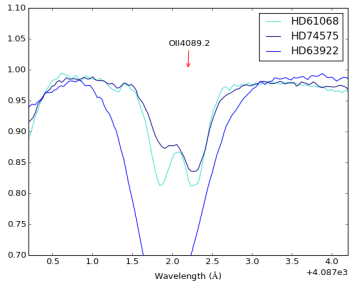
HD61068
HD74575
HD63922
OII4089.2
Wavelength (Å)
+4.087e3

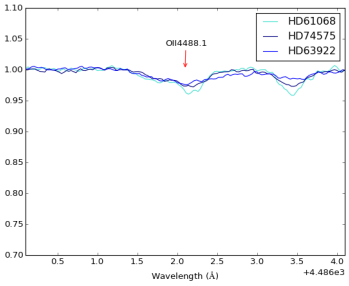
HD61068
HD74575
HD63922
OII4488.1
Wavelength (Å)
+4.486e3

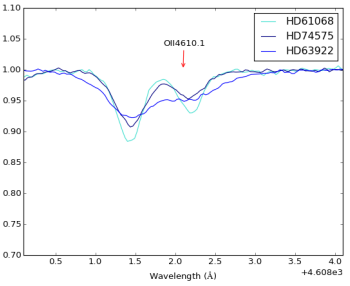
HD61068
HD74575
HD63922
OII4610.1
Wavelength (Å)
+4.608e3

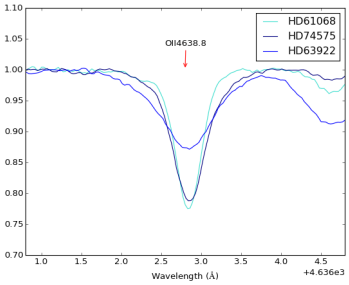
HD61068
HD74575
HD63922
OII4638.8
Wavelength (Å)
+4.636e3

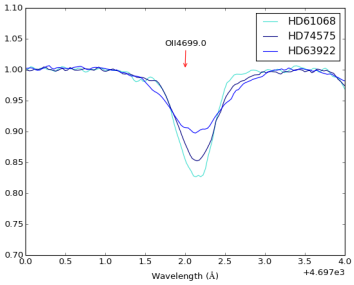
HD61068
HD74575
HD63922
OII4699.0
Wavelength (Å)
+4.697e3

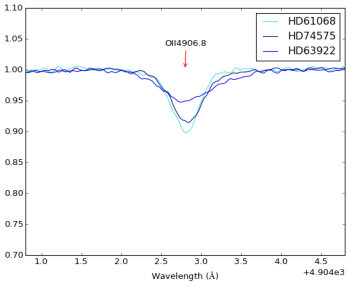
HD61068
HD74575
HD63922
OII4906.8
Wavelength (Å)
+4.904e3

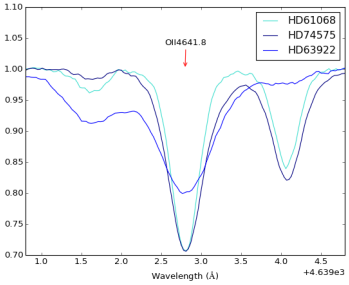
HD61068
HD74575
HD63922
OII4641.8
Wavelength (Å)
+4.639e3

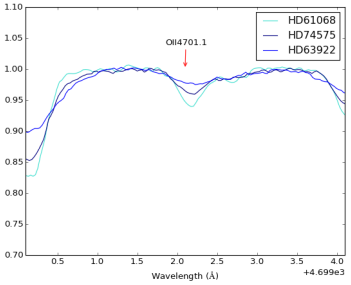
HD61068
HD74575
HD63922
OII4701.1
Wavelength (Å)
+4.699e3

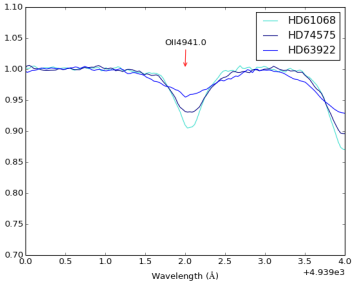
HD61068
HD74575
HD63922
OII4941.0
Wavelength (Å)
+4.939e3

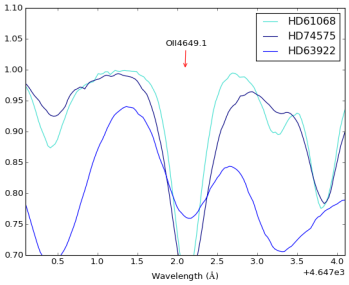
HD61068
HD74575
HD63922
OII4649.1
Wavelength (Å)
+4.647e3

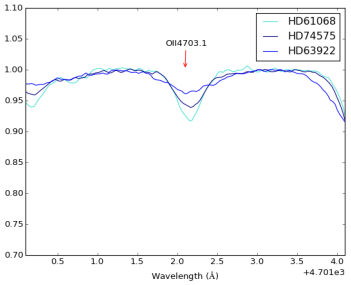
HD61068
HD74575
HD63922
OII4703.1
Wavelength (Å)
+4.701e3

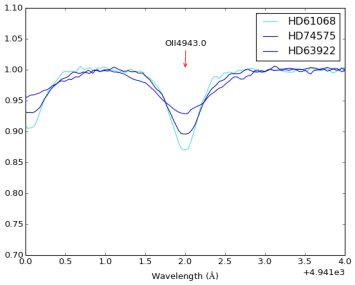
HD61068
HD74575
HD63922
OII4943.0
Wavelength (Å)
+4.941e3

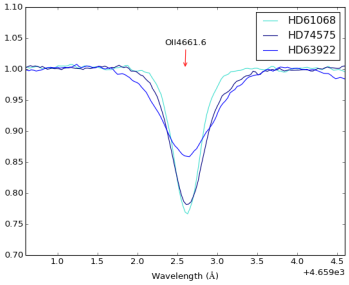
HD61068
HD74575
HD63922
OII4661.6
Wavelength (Å)
+4.659e3

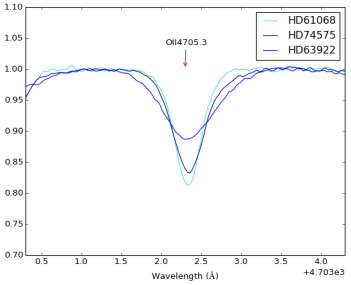
HD61068
HD74575
HD63922
OII4705.3
Wavelength (Å)
+4.703e3

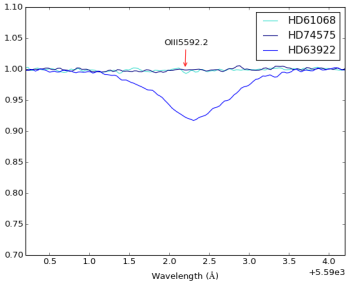
HD61068
HD74575
HD63922
OIII5592.2
Wavelength (Å)
+5.59e3

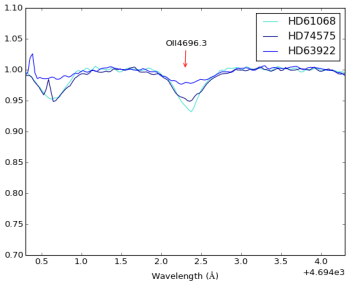
HD61068
HD74575
HD63922
OII4696.3
Wavelength (Å)
+4.694e3

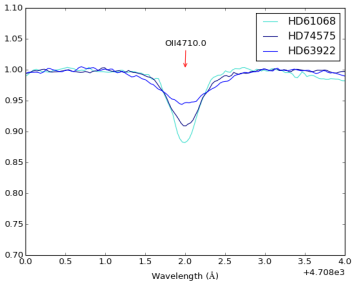
HD61068
HD74575
HD63922
OII4710.0
Wavelength (Å)
+4.708e3

Appendix C

$\log gf$ differences in the example of HIP34499

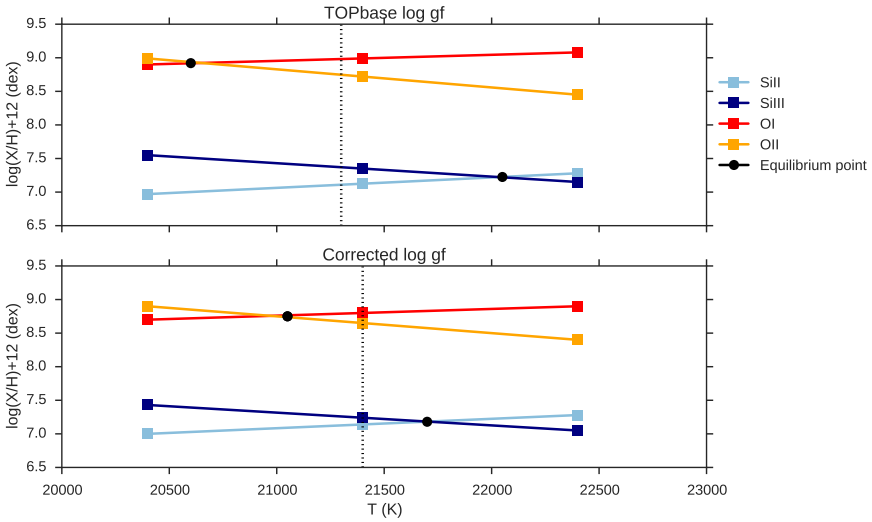

Figure C.1: HIP34499 ionization equilibrium for silicon and oxygen with the `TOPbase` and corrected $\log gf$ values.

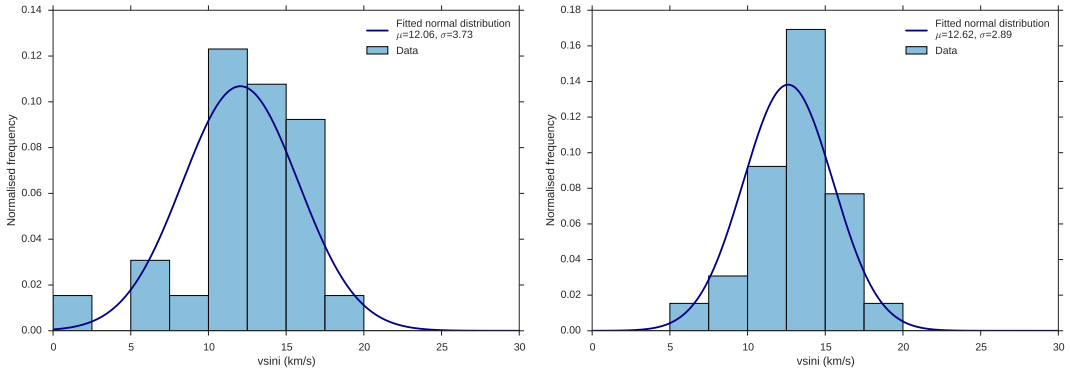

(a) with the TOPbase $\log gf$ (b) with the corrected $\log gf$

Figure C.2: HIP34499 $v \sin i$ estimation before and after $\log gf$ corrections

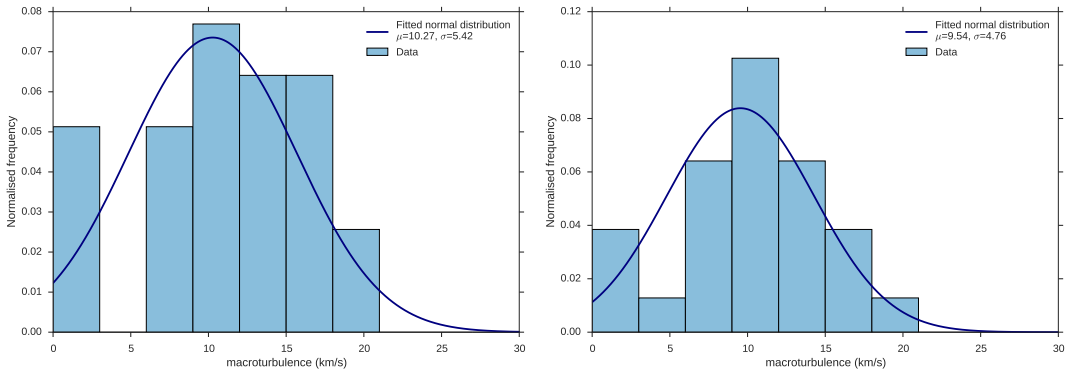

(a) with the `TOPbase` $\log gf$ (b) with the corrected $\log gf$

Figure C.3: HIP34499 macroturbulence estimation before and after $\log gf$ corrections

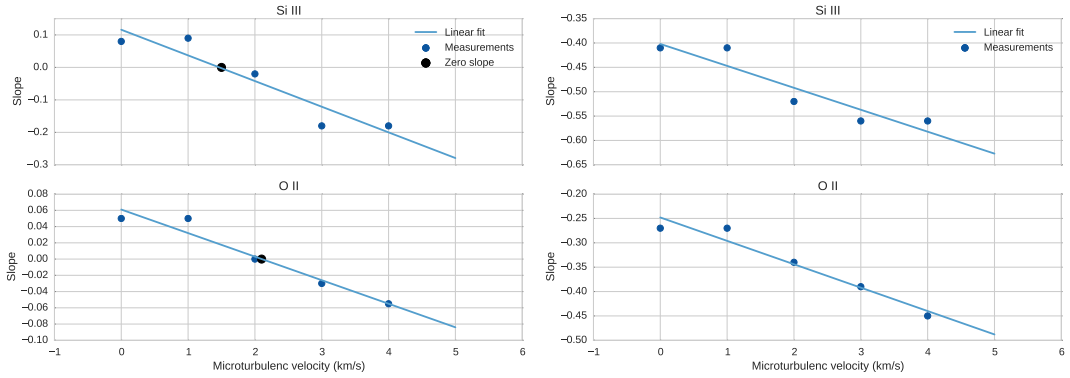

(a) with the `TOPbase` $\log gf$ (b) with the corrected $\log gf$

Figure C.4: HIP34499 microturbulence estimation with the `TOPbase` and corrected $\log gf$

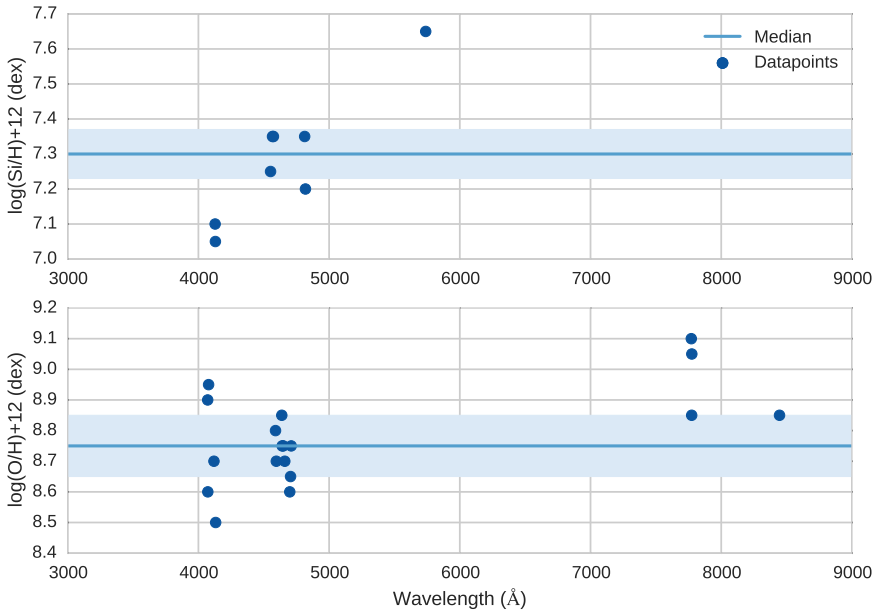

(a) with the `TOPbase` $\log gf$

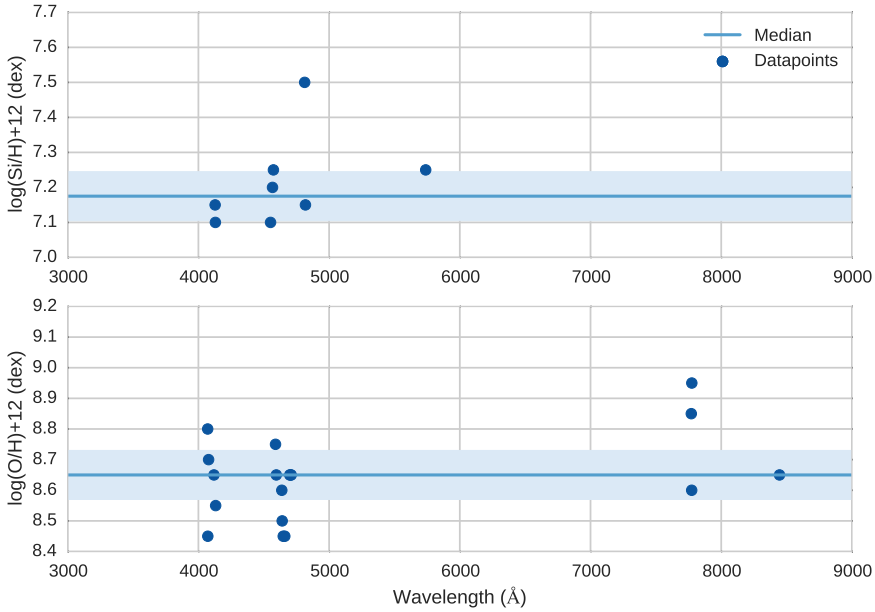

(b) with the corrected $\log gf$

Figure C.5: HIP34499 Si and O abundance estimation before and after $\log gf$ corrections

Appendix D

Line-by-line Si and O abundances for analysed stars

Table D.1: Silicon lines used for abundance determination

	SiII					SiIII						SiIV	
HIP	4128.07	4130.09	5041.02	5055.98	6347.11	6371.37	4552.62	4567.84	4574.76	4716.55	4813.33	4819.71	4828.95	5739.73	4088.86	4116.1	4654.31
37036	7.55	7.55	-	-	-	-	7.55	7.60	7.60	7.55	7.50	7.50	7.50	7.65	7.70	7.70	-
38164	-	-	-	-	-	-	7.55	7.55	7.55	-	-	7.65	7.60	7.25	-	7.70	-
42828	7.45	7.50	7.50	-	7.45	7.60	7.50	7.50	7.50	7.55	7.55	7.50	7.55	7.60	-	-	-
36615	7.45	7.55	-	-	-	-	7.5	7.55	7.55	7.55	7.5	-	7.4	7.6	7.6	7.4	-
39540	-	-	-	-	-	-	7.35	7.40	7.45	7.55	7.30	-	7.40	7.45	-	7.30	-
50067	7.35	7.25	7.20	7.50	7.50	7.50	-	7.25	7.35	-	-	-	-	7.25	-	-	-
29417	7.30	7.20	-	-	-	-	7.25	7.35	7.40	-	7.70	-	-	7.40	-	-	-
42357	7.55	7.50	7.40	7.50	-	-	-	7.45	7.65	-	-	-	-	-	-	-	-
14898*	7.70	7.70	7.50	-	7.95	7.90	-	-	-	-	-	-	-	-	-	-	-
34325	-	-	-	-	-	-	7.25	7.40	7.45	7.50	7.30	7.30	7.45	-	7.50	7.30	-
33611	7.30	7.20	-	-	-	-	7.15	7.30	7.40	-	-	-	7.50	7.25	-	-	-
29678	7.65	7.40	-	-	-	-	7.25	7.40	7.50	7.65	7.55	-	7.40	7.45	7.50	7.55	-
39774	7.40	7.35	-	-	-	-	7.30	7.30	7.25	-	-	-	-	-	-	-	-
46760	7.40	7.25	-	-	-	-	7.15	7.35	7.45	-	7.60	7.40	7.50	7.30	-	7.55	-
29217	7.50	7.35	-	-	-	-	7.20	7.30	7.35	7.55	7.40	7.30	7.45	7.40	-	-	-
25582	7.50	7.35	-	7.30	-	-	7.35	7.40	7.60	-	-	7.30	-	7.55	-	-	-
34499	7.15	7.10	-	-	-	-	7.10	7.20	7.25	-	7.50	7.15	-	7.25	-	-	-

Table D.2: Oxygen lines used for abundance determination

	OI						OII								
HIP	6155.9	6156.7	6158.1	7771.9	7774.1	7775.3	8446.3	4062.9	4071.2	4072.1	4078.8	4083.9	4085.1	4087.1	4089.2	4092.9	4119.2	4129.3	4132.8
37036	-	-	-	8.75	8.80	8.85	-	8.75	8.75	8.75	8.75	8.75	8.95	8.8	-	8.90	8.75	8.75	8.70
38164	-	-	-	-	-	-	-	8.75	-	-	8.90	-	-	8.80	-	8.95	8.90	-	8.95
42828	-	-	-	8.65	-	8.80	8.75	8.75	8.75	8.80	8.70	-	-	-	-	8.70	8.70	8.75	8.65
36615	-	-	-	8.70	-	8.65	-	8.65	8.60	8.80	8.75	8.65	-	8.65	-	8.75	8.65	8.70	8.70
39540	-	-	-	-	-	-	-	8.65	8.65	8.80	8.80	8.65	-	8.60	-	8.80	8.70	8.85	8.80
50067	8.55	8.65	8.60	8.70	8.70	8.80	-	-	-	8.65	8.75	-	-	-	-	-	8.70	-	-
29417	-	8.70	8.70	8.95	8.75	8.85	8.85	-	-	8.70	8.70	8.80	8.80	-	8.95	-	8.65	-	-
42357	8.60	8.70	8.65	8.65	-	8.70	-	-	-	-	-	-	-	-	-	-	-	-	-
14898*	8.85	8.85	8.85	9.00	8.80	8.90	8.80	-	-	-	-	-	-	-	-	-	-	-	-
34325	-	-	-	-	-	-	-	8.65	8.60	8.70	8.75	8.75	-	8.65	-	8.80	8.65	8.65	8.75
33611	-	-	8.65	8.85	8.65	8.85	8.75	-	8.95	8.65	8.65	8.85	8.90	8.80	-	8.75	8.65	-	-
29678	-	-	-	8.85	8.55	8.80	-	8.80	8.75	8.80	8.75	8.80	8.90	8.75	8.60	8.80	8.65	8.80	8.80
39774	-	-	-	8.50	-	8.65	8.80	-	-	8.75	-	-	-	-	-	-	-	-	-
46760	-	-	-	8.70	8.75	8.80	8.70	-	8.85	8.65	8.65	8.90	-	8.75	-	8.65	8.55	8.80	8.60
29127	-	-	-	8.75	-	-	-	8.80	8.85	8.75	8.80	-	-	8.85	-	-	8.60	8.70	8.70
25582	-	-	-	9.05	8.75	8.95	8.75	-	-	8.80	-	-	-	-	-	-	-	-	-
34499	-	-	-	8.85	8.60	8.95	8.65	-	8.80	8.45	8.70	-	-	-	-	-	8.65	-	8.55

Table D.3: Oxygen lines used for abundance determination cont.

	OII																OIII
HIP	4488.1	4590.9	4596.1	4602	4609.3	4610.1	4638.8	4641.8	4649.1	4661.6	4696.3	4699	4701.1	4703.1	4705.3	4710	4906.8	4941	4943	5592.2
37036	-	8.75	8.80	8.65	8.75	8.75	8.75	8.75	9.05	8.75	-	8.65	-	8.70	8.75	8.75	8.70	8.75	8.75	-
38164	-	8.75	8.80	-	-	-	8.75	8.80	8.75	8.80	-	8.75	-	8.90	8.75	8.85	8.80	8.75	8.75	8.70
42828	-	8.75	8.75	-	-	8.75	8.80	8.80	8.80	8.75	-	8.70	8.70	8.70	8.80	8.65	8.70	8.75	8.75	-
36615	-	8.60	8.65	-	8.65	8.60	-	-	8.65	-	-	-	8.65	8.60	8.65	8.65	8.65	8.50	8.60	-
39540	-	8.65	8.70	8.60	8.70	8.70	8.75	8.70	8.65	8.69	-	-	8.70	8.65	8.65	8.75	8.70	8.60	8.70	-
50067	-	8.85	8.95	-	-	-	8.70	8.60	8.45	8.60	-	-	-	-	8.80	-	-	-	-	-
29417	-	8.80	8.85	-	-	-	8.70	8.60	8.60	8.55	-	-	-	-	9.00	8.80	-	-	-	-
42357	-	-	-	-	-	-	-	8.55	8.70	-	-	-	-	-	-	-	-	-	-	-
14898*	-	-	-	-	-	-	-	-	-	-	-	-	-	-	-	-	-	-	-	-
34325	-	8.65	8.70	-	-	-	8.65	8.60	8.55	8.65	-	8.65	-	-	8.65	8.70	8.75	8.60	8.68	-
33611	-	8.75	8.80	-	-	-	8.65	8.55	8.55	8.55	-	-	-	-	8.90	8.80	-	-	-	-
29678	-	8.75	8.75	8.70	8.85	8.85	8.70	8.70	8.65	8.65	-	8.80	8.90	8.80	8.80	8.75	8.75	8.70	8.85	-
39774	-	-	-	-	-	-	8.80	8.60	8.55	-	-	-	-	-	-	-	-	-	-	-
46760	-	8.65	8.75	8.70	8.85	-	8.60	8.55	8.55	8.50	-	8.65	-	8.80	8.90	8.70	-	8.70	-	-
29127	-	8.75	8.80	-	-	-	8.80	8.70	8.60	8.65	-	8.80	8.75	8.80	8.85	8.90	8.75	-	-	-
25582	-	8.95	-	-	-	-	8.75	8.60	8.65	8.65	-	-	-	-	8.80	-	-	-	-	-
34499	-	8.75	8.65	-	-	-	8.60	8.50	8.45	8.45	-	8.65	-	-	8.65	8.65	-	-	-	-